

Evaluating cell cycle- and autophagy-associated cellular accumulation of lipid-based nanoparticles

Received: 8 March 2024

Accepted: 10 June 2025

Published online: 01 July 2025



Yisha Wang^{1,6}, Gan Luo^{1,6}, Haiyang Wang^{1,6}, Yue Zheng¹, Xiao Xu², Wenbin Zhou¹, Junrong Lin¹, Baocheng Chen¹, Yangfu Guo^{1,3}, Yifeng Jin¹ & Meihua Sui^{1,4,5}✉

Little is known about how cell cycle and autophagy, two fundamental life processes, affect cellular accumulation of nanoparticles. What's even more tough is that several long-lasting methodological barriers have hindered the progress of related research. Here we firstly show the construction of a multi-functional platform for overcoming existing methodological obstacles through integrating multiple technical approaches including *autophagy-related gene 7* knockout to specifically block autophagy, PIP-FUCCI transfection and mitotic shake-off to thoroughly separate cell cycle phases, and 3D reconstruction to stereoscopically evaluate cellular accumulation of nanoparticles. Further application of this platform reveals that after a 2-hour incubation of lipid-based nanoparticles, G2-phase and M-phase cells, two populations previously muddled up together as G2/M-phase cells, respectively exhibited the maximum and minimum nanoparticle accumulation. Meanwhile, our data preliminarily suggest enhanced nanoparticle accumulation by autophagy blockade. Besides cell cycle and autophagy, comprehensive statistical analyses reveal a close association between cellular accumulation of nanoparticles and nanoparticle type. This study not only provides a valuable technical strategy, but uncovers important characteristics of cellular accumulation of nanoparticles, offering new insights for optimization and application of nanomedicines.

Leveraging the distinctive surface and size effect, nanodrugs have a wide range of applications in biomedicine¹. Among a variety of nanocarriers, lipid-based nanoparticles, e.g., liposomes (LIP) and lipid nanoparticles (LNP), serve as exemplary carriers for successful clinical translation². For instance, Doxil®, doxorubicin utilizing LIP as the carriers, is the first nano-sized drug approved for patients³. Comirnaty®, the first LNP-delivered mRNA vaccine, is extensively used worldwide⁴. It has been noted that nanoparticle accumulation

could be affected by key cellular properties. Cell cycle, a fundamental life process of mammalian cells, is critically involved in the onset, development, treatment response and prognosis of many diseases⁵. Notably, proliferating tumor cells inside tumor tissues are distributed at distinct cell cycle phases, which is called cell cycle heterogeneity⁶. Given that studies from our team and others demonstrate that tumor cells possess cell cycle-dependent sensitivity to a variety of treatments including nano-drugs, cell cycle

¹School of Basic Medical Sciences and Sir Run Run Shaw Hospital, Zhejiang University School of Medicine, Hangzhou, China. ²School of Clinical Medicine, Hangzhou Medical College, Hangzhou, China. ³School of Basic Medical Sciences, Henan University, Kaifeng, China. ⁴Shaoxing People's Hospital (Shaoxing Hospital, Zhejiang University School of Medicine), Shaoxing, China. ⁵Cancer Center, Zhejiang University, Hangzhou, China. ⁶These authors contributed equally: Yisha Wang, Gan Luo, Haiyang Wang. ✉e-mail: suim@zju.edu.cn

heterogeneity has been considered as a big challenge for antitumor therapy^{6–10}.

Nevertheless, so far only five relevant literatures explored the impact of cell cycle on the retention of inorganic nanoparticles, including CdTe and CdSe QDs^{11–14}, as well as ZnO¹⁵. Regarding organic nanoparticles, seven previous literatures respectively investigated the cell cycle-associated accumulation of carboxylated polystyrene nanoparticles (PS-COOH), FITC-dextran fibroin-encapsulated microspheres, cRGD-targeting matrix metalloproteinase-sensitive nanoparticles (FITC@NPs-cRGD), folate modified poly (L-amino acid) micelles and Tat/pGL3-Ca²⁺ nanoparticles^{16–22}. It is notable that these reports yielded inconsistent results on cell cycle-associated nanoparticle accumulations. For instance, although cellular accumulation of CdTe QDs^{11,12}, ZnO¹⁵, PS-COOH¹⁶ and FITC-dextran fibroin-encapsulated microspheres¹⁹ exhibited similar cell cycle-associated characteristics ($G1 < S < G2/M$), FITC@NPs-cRGD showed a reverse accumulation ranking ($G2/M < S < G1$)²⁰. These discrepancies may be attributed to the following long-lasting methodological limitations: (i) the methods previously used could not differentiate between G2-phase and M-phase cells in physiological state^{11–22}; (ii) cell dissociation agents (e.g., trypsin)^{11,14–21}, exogenous stimuli (e.g., serum deprivation)^{16,17,20,22} and “cell cycle blockers” (e.g., nocodazole)^{11,15,17,20–22} for artificial synchronization of cell cycle, inevitably disturbed the cellular physiology and nanoparticle accumulation; (iii) evaluation of nanoparticle accumulation with confocal laser scanning microscopy (CLSM) was limited at a two-dimensional (2D) level, in which cell geometric characteristics and heterogeneous intracellular distribution of nanoparticles were ignored^{11–13,16,21,22}. Indeed, these technical barriers have become “bottleneck” problems preventing deeper and further investigations in related scientific research and development.

Autophagy is another fundamental biological process involved in the maintenance of physiological homeostasis and pathogenesis of a wide range of diseases²³. Interestingly, recent studies indicate that cancer cells are more dependent on autophagy than normal cells, with high levels of endogenous autophagy detected in various types of cancers such as osteosarcoma and pancreatic cancer^{24,25}. It has been revealed that evolutionarily conserved autophagy-related genes (ATG) are core regulatory genes of autophagy^{23,26}. Moreover, the endosomal/lysosomal system, which is critically involved in nanoparticle accumulation²⁷, also plays a pivotal role in autophagy²⁸. As a result, there is a growing body of literature relevant to “nano-autophagy” interactions, which mainly focused on the possible capability of nanoparticles to induce autophagy per se²⁹. To date, only four previous reports explored the potential effect of autophagy on cellular accumulation of nanoparticles, all measured at 2D level^{30–33}. Among these studies, Fageria et al. reported a reduced cellular accumulation of Ag nanoparticles upon chloroquine treatment³⁰, and Sipos et al. observed a suppressed cellular accumulation of polystyrene nanoparticles after exposure to 3-methyladenine and bafilomycin A1^{31,32}. However, co-loading of 3-methyladenine into hyaluronic acid-modified MIL-125-Ti nanoparticles containing doxorubicin-vitamin E succinate prodrug (HA-MIL125@DV) led to significantly increased nanoparticle accumulation in both MCF-7 and MCF-7/ADR cell lines, a pair of drug-sensitive and multidrug-resistant cell lines³³. It is notable that, as non-specific autophagy inhibitors (e.g., chloroquine, 3-methyladenine and bafilomycin A1) were used to modulate autophagy in these studies, the obtained data may be confounded by non-autophagy-related pharmacological effects induced by these non-specific inhibitors^{34,35}.

In this study, inspired by our strong curiosities on the impacts of cell cycle and endogenous autophagy on cellular accumulation of nanoparticles, and by the methodological challenges existed in research on “nano-cell cycle/autophagy” interactions, a pair of isogenic cancer cell lines including wild type (WT) strain and *autophagy-related gene 7* knockout (ATG7 KO) derivative is firstly used to eliminate the possible interference caused by non-specific autophagy inhibitors.

Next, by combining transfection of the cell cycle-indicating PIP-FUCCI plasmid³⁶ and mitotic shake-off³⁷, a thorough distinguishment of cells at four distinct cell cycle phases under physiological conditions is successfully achieved. Further integration of high-resolution CLSM and three-dimensional (3D) reconstruction techniques enables multi-dimensional evaluations on cellular accumulation of fluorescence-labeled nanoparticles. Importantly, by using this valuable technical platform, nanoparticle accumulation after a 2-hour incubation of LIP of Doxil® and LNP of Comirnaty® have been initially and parallelly characterized at four distinct cell cycle phases and under specific autophagy status in WT and ATG7 KO PIP-FUCCI cancer cells. Moreover, the correlations among total fluorescence intensity (TFI) and mean fluorescence intensity (MFI) at both 2D and 3D levels, four key parameters utilized in this promising platform for measuring nanoparticle accumulation, have been carefully evaluated.

Results

Synthesis and characterization of model nanoparticles DiD-LIP and DiD-LNP

Despite the wide application of LIP and LNP as drug carriers, our understanding on their “nano-bio” interactions are far from sufficient. So far, no literature has investigated the potential impact of either cell cycle or autophagy on the cellular accumulation of LIP or LNP. Hereby, LIP and LNP were respectively synthesized according to officially published formulations^{38,39} and our previous report⁴, with DiD as a tracer fluorescence^{40,41}. Briefly, DiD-LIP was formulated by hydrating a lipid mixture containing HSPC, cholesterol, mPEG₂₀₀₀-DSPE and DiD in sucrose-histidine buffer, followed by downsizing using a 10-mL extruder barrel (Fig. 1a left). DiD-LNP was prepared with a microfluidic mixing device through mixing the ethanol phase containing ALC-0315, DSPC, cholesterol, ALC-0159, DiD and the aqueous phase containing firefly luciferase mRNA (LUC mRNA) to enhance the stability of LNP^{4,42} (Fig. 1a right).

Further characterization with dynamic light scattering (DLS) showed that the Z-average/PDI of DiD-LIP and DiD-LNP were 104.433 ± 0.513 nm/ 0.102 ± 0.036 and 106.767 ± 0.306 nm/ 0.145 ± 0.009 , respectively (Fig. 1b). Additional cryogenic transmission electron microscopy (Cryo-TEM) examination confirmed that DiD-LIP was characterized as hollow spheres, whereas DiD-LNP exhibited a typical electron-dense core structure containing LUC mRNA (Fig. 1c, insert)⁴. Zeta potentials of DiD-LIP and DiD-LNP were -29.100 ± 2.081 mV and 3.660 ± 0.476 mV, respectively (Fig. 1c). These data demonstrate that both model nanoparticles possess highly monodisperse particle-size distribution and weak surface charge.

Importantly, DiD-LIP and DiD-LNP exhibited good stability when stored in phosphate buffer saline (PBS) at 4 °C, without remarkable changes detected for Z-average or PDI from Day 1 to Day 28 (Supplementary Fig. 1a, b and Supplementary Fig. 2), or in DMEM medium containing 10% fetal bovine serum (FBS) at 37 °C for up to 24 h (simulating the experimental environment) (Fig. 1d, e and Supplementary Fig. 3). Both DiD-LIP and DiD-LNP displayed a single and size-stable intensity peak throughout the whole incubation period and under two distinct physiological conditions. Moreover, the standard curves of phospholipid and corresponding equations were obtained for further dosage determination of DiD-LIP and DiD-LNP (see “Methods”, Supplementary Fig. 1c, d)⁴.

Establishment of a multi-functional technical platform for determining cell cycle- and autophagy-associated cellular accumulation of nanoparticles

Using an empty vector as a control, the isogenic WT and ATG7 KO U2OS cell lines we previously obtained were transduced with lentiviral particles carrying the cell cycle-indicating PIP-FUCCI plasmid (see “Methods”). After screening with G418 and flow cytometry, corresponding WT and ATG7 KO PIP-FUCCI cell lines expressing strong

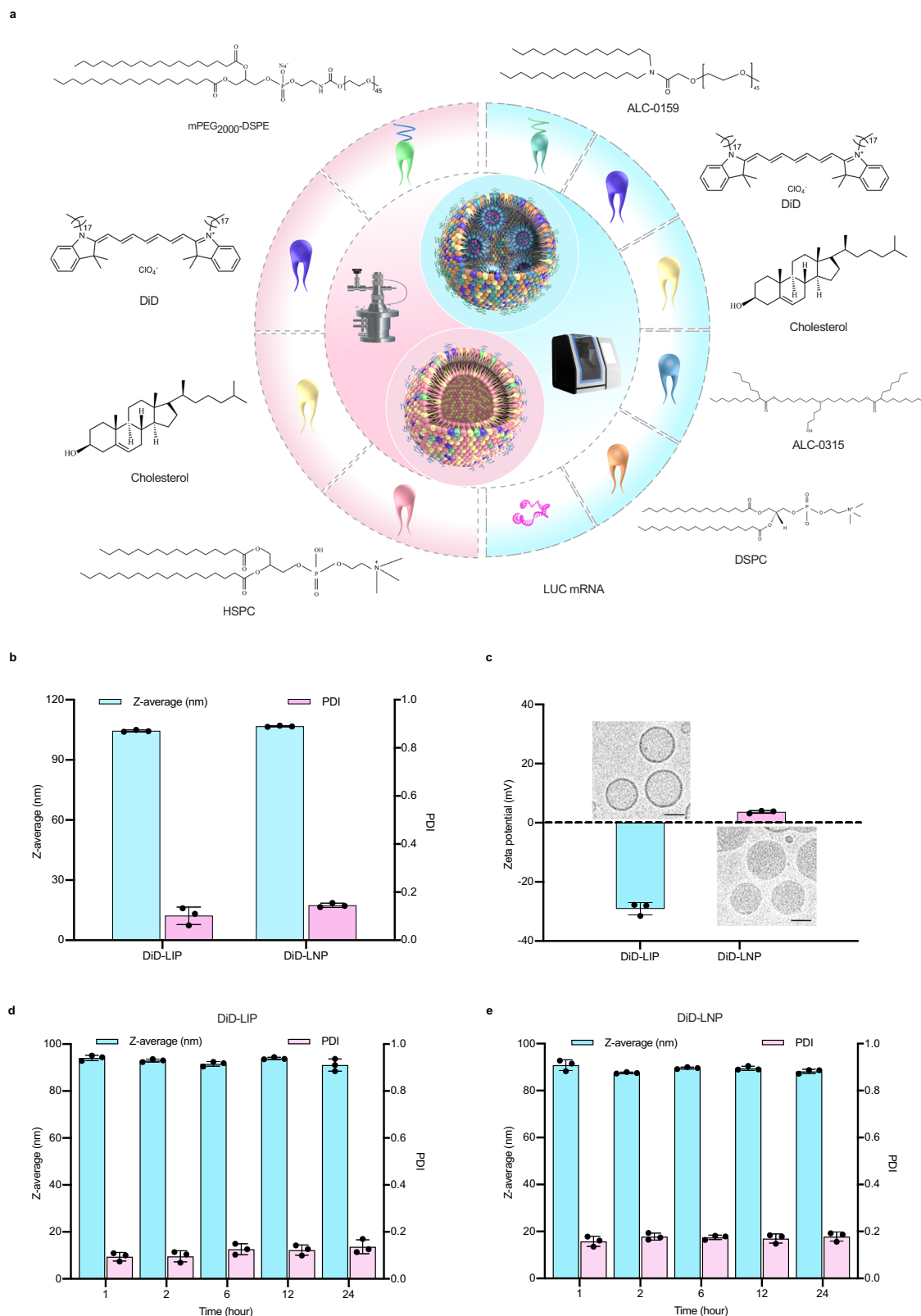


Fig. 1 | Preparation and characterization of DiD-labeled liposomes (DiD-LIP) and lipid nanoparticles (DiD-LNP). **a** Schematic illustration of the synthesis of DiD-LIP (left, pink background) and DiD-LNP (right, blue background). For detailed synthesis procedures, please refer to the “Methods”. **b** Z-average and polydispersity index (PDI) of DiD-LIP and DiD-LNP. **c** Zeta potentials of DiD-LIP and DiD-LNP, with representative Cryo-TEM images (inserts) selected from 15 randomly chosen fields. Scale bars, 50 nm. **d, e** Z-average and PDI of DiD-LIP and DiD-LNP in DMEM containing 10% FBS stored at 37 °C for up to 24 h. Data in (**b–e**) were

presented as mean \pm SD ($n = 3$ independent biological replicates). Z-average and PDI among various time points were evaluated by one-way ANOVA, showing no statistically significant difference at $\alpha = 0.05$ level: the Z-average of DiD-LIP showed $F(4, 10) = 2.865$, $p = 0.081$, $\eta^2 = 0.534$; the PDI of DiD-LIP showed $F(4, 10) = 1.968$, $p = 0.176$, $\eta^2 = 0.440$; the Z-average of DiD-LNP showed $F(4, 10) = 3.482$, $p = 0.050$, $\eta^2 = 0.582$; the PDI of DiD-LNP showed $F(4, 10) = 0.698$, $p = 0.611$, $\eta^2 = 0.218$. The level of significance was set at $p < 0.05$. Source data are provided as a Source Data file.

mVenus (green fluorescence) and/or mCherry (red fluorescence) were successfully constructed (Fig. 2a). PIP-FUCCI transfection and subsequent selection with G418 had a marginal influence on cellular morphology and proliferation rate (Supplementary Figs. 4 and 5).

However, although single positivity of mVenus and mCherry could respectively indicate cells at G1-phase and S-phase, both G2-phase and M-phase cells are mVenus and mCherry double-positive and exhibit yellow fluorescence (overlap of green and red). That is, PIP-FUCCI transfection by itself cannot distinguish between G2-phase and M-phase cells in situ. Fortunately, different from G1-phase, S-phase and G2-phase cells naturally adhering to the culture dish with polyhedral shapes, typical M-phase cells have unique properties such as spherical shape⁴³, significantly reduced adhesion capability and floating state in culture media due to “mitotic rounding”⁴⁴. These properties have led to a well-recognized approach being used for more than half a century⁴⁵, which is called mitotic shake-off³⁷, for convenient collection of M-phase cells with minimal physiological disturbance to the cells⁴⁶. Enlightened by these characteristics, we hereby combined PIP-FUCCI transfection, mitotic shake-off and morphological examination of mitotic cells to establish a strategy for thorough distinguishment of the four cell cycle phases. In addition, cell membrane labeling with FITC-EpCAM prior to mitotic shake-off assisted in the exclusion of apoptotic cells and cellular debris via drawing the outline of the cell membrane (see “Methods”; Fig. 2b, highlighted with dashed frame).

Importantly, to address potential concerns regarding the possibility that M-phase cells identified by the integrated approach might be mixed with just divided G1-phase cells having not fully re-adhered onto the culture dish, we performed time-lapse live-cell imaging with naturally growing WT and *ATG7* KO PIP-FUCCI cells for up to 25 h (estimated cell doubling time, Supplementary Fig. 5). Our data showed that due to the rapid decay of mCherry protein, just divided G1-phase cells quickly became mVenus single-positive displaying green nuclear fluorescence (within 5 min after division), which were distinguishable from pre-division mitotic cells displaying yellow nuclear fluorescence³⁶ (Supplementary Figs. 6 and 7). These data confirmed the high specificity and sensitivity of PIP-FUCCI in indicating different cell cycle phases. In addition, flow cytometric analysis for DNA quantification was conducted to further confirm that the M-phase cells identified in this study were truly mitotic cells without splitting their DNA. Impressively, the obtained data revealed that $90.00 \pm 2.69\%$ and $91.80 \pm 2.43\%$ of double-positive floating cells collected via mitotic shake-off (cells analyzed as M-phase cells) exhibited 4 N DNA content in WT and *ATG7* KO PIP-FUCCI cells, respectively (Supplementary Fig. 8 and Supplementary Table 1). It is noteworthy that in previous literature, even toxic mitosis-arresting agents induced a lower percentage of cells arrested at M phase or G2/M phase (52–90%), which were considered and further analyzed as mitotic cells^{11,47–50}. Taken together, these data have provided multiple lines of evidence supporting the successful collection and identification of M-phase cells for further evaluation.

Further integration of high-resolution CLSM and 3D reconstruction technique significantly strengthened this multi-functional platform for determining cell cycle- and autophagy-associated nanoparticle accumulation (Fig. 2b). Using a 2 h incubation of DiD-LIP (blue fluorescence) as a representative model, this platform could characterize nanoparticle accumulation not only at different dimensional levels, but at four distinct cell cycle phases respectively in WT and *ATG7* KO PIP-FUCCI cells (Fig. 2c). As mentioned above, Z-axis scanning and subsequent 3D reconstruction with CLSM were integrated into this platform to overcome the limitations of 2D imaging where fluorescence signals vary across sections. Given that CLSM effectively shields out-of-focus background and significantly enhances the clarity of fluorescent signals⁵¹, the intracellular total fluorescence intensity measured by CLSM and subsequent 3D reconstruction

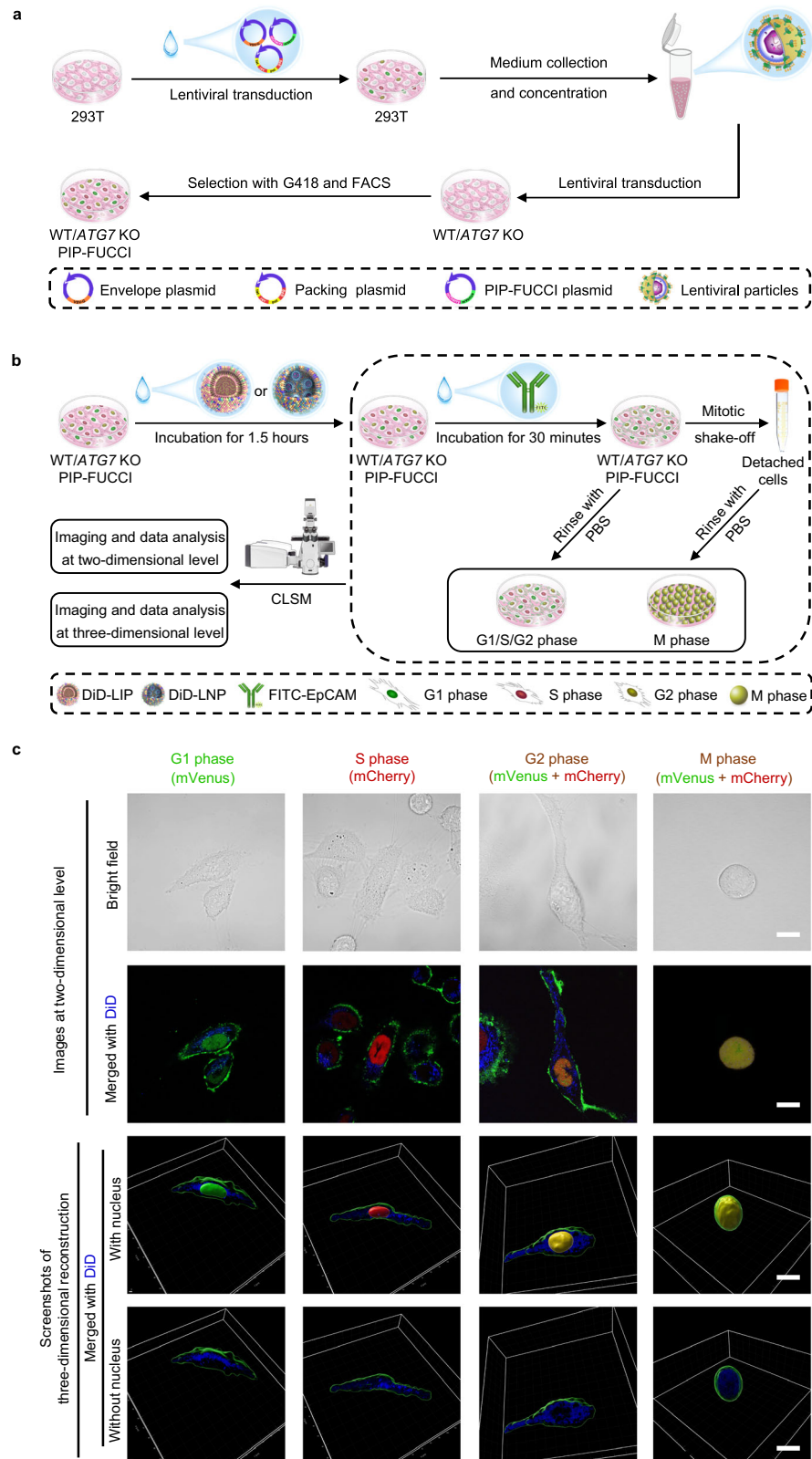
should be consistent irrespective of cell shape and culture status (adherent or floating) upon detection. Nevertheless, to confirm this technical reliability, after a 2 h incubation of nanoparticles, WT and *ATG7* KO PIP-FUCCI cells were dissociated with trypsinization to obtain floating G1-phase, S-phase, G2-phase and M-phase cells for subsequent DiD fluorescence intensity detection with CLSM (see the below section “Determination of cell cycle- and endogenous autophagy-associated cellular accumulation of DiD-LIP”).

In brief, this platform has multiple superiorities including complete and thorough separation and collection of alive cells at four cell cycle phases, elimination of interferences caused by “extra” treatments (e.g., cell dissociation agents, cell cycle synchronization drugs, non-specific autophagy inhibitors), and capability for parallel investigations on multiple biological parameters/dimensions.

Little influence of DiD-LIP and DiD-LNP per se on cell cycle distribution and autophagy of WT and *ATG7* KO PIP-FUCCI cell lines

To clarify the impact of cell cycle and autophagy on nanoparticle accumulation, the possible interference of model nanoparticles on cancer cells per se needs to be firstly excluded. Therefore, WT and *ATG7* KO PIP-FUCCI cells were respectively treated with DiD-LIP and DiD-LNP for further evaluation. As depicted in Fig. 3a, and Supplementary Table 2, flow cytometry analyses showed that percentages of nanoparticle-untreated cancer cells at G1 phase, S phase, G2 phase and M phase were $33.10 \pm 1.77\%$, $54.83 \pm 2.82\%$, $11.81 \pm 0.93\%$ and $0.26 \pm 0.19\%$, respectively, for WT PIP-FUCCI cell line, and $31.30 \pm 2.21\%$, $54.22 \pm 2.49\%$, $13.94 \pm 1.29\%$ and $0.53 \pm 0.16\%$, respectively, for *ATG7* KO PIP-FUCCI cell line. Percentages of DiD-LIP-treated WT and *ATG7* KO PIP-FUCCI cell lines at G1 phase, S phase, G2 phase and M phase were $33.18 \pm 2.08\%$, $54.64 \pm 3.14\%$, $11.92 \pm 1.09\%$ and $0.26 \pm 0.17\%$, respectively, and $31.25 \pm 2.15\%$, $53.99 \pm 2.37\%$, $14.29 \pm 0.57\%$, $0.48 \pm 0.10\%$, respectively. Correspondingly, the cell cycle distributions of DiD-LNP-treated WT and *ATG7* KO PIP-FUCCI cell lines at G1 phase, S phase, G2 phase and M phase were $33.70 \pm 2.36\%$, $54.38 \pm 3.37\%$, $11.66 \pm 0.92\%$ and $0.27 \pm 0.21\%$, respectively, and $31.15 \pm 0.61\%$, $55.02 \pm 1.58\%$, $13.27 \pm 1.44\%$ and $0.56 \pm 0.16\%$, respectively. Importantly, further statistical analyses demonstrated that no matter with or without 2 h nanoparticle treatment, no significant difference on cell cycle distribution was observed in WT and *ATG7* KO PIP-FUCCI cells (Supplementary Table 2). Moreover, data obtained with additional regular flow cytometry assay (without mitotic shake-off) at longer time points demonstrated that in both WT and *ATG7* KO PIP-FUCCI cell lines, neither DiD-LIP nor DiD-LNP exhibited significant influence on general cell cycle distribution after incubation for 12, 24, and 48 h, respectively (Supplementary Figs. 9 and 10, Supplementary Tables 3 and 4).

Previous studies demonstrate that *ATG7* knockdown effectively blocked cellular autophagy⁵². Indeed, although autophagic vesicles (AVs, including autophagosomes and autophagic lysosomes) with typical double-layer membrane structure were easily observed in WT PIP-FUCCI cells with TEM, no typical AVs were seen in *ATG7* KO PIP-FUCCI cells (Fig. 3b). Further statistical analyses confirmed significantly fewer AVs in *ATG7* KO PIP-FUCCI cells than in WT PIP-FUCCI cells (Fig. 3c and Supplementary Table 5). As anticipated, *ATG7* protein level was high in WT PIP-FUCCI cells while undetectable in *ATG7* KO PIP-FUCCI cells in Western blotting (Fig. 3d). Moreover, the LC3-II/LC3-I ratio, which is positively correlated with the autophagy level⁵³, was significantly decreased in *ATG7* KO PIP-FUCCI cells. In contrast, p62, which is negatively correlated with autophagy⁵³, was dramatically increased in *ATG7* KO PIP-FUCCI cells. Our data firmly demonstrated the successful blockade of autophagy in *ATG7* KO PIP-FUCCI cells. Encouragingly, neither DiD-LIP nor DiD-LNP exhibited any effect in the aforementioned assays, indicating that the designated nanoparticle treatment had a marginal impact on the autophagy of WT and *ATG7* KO PIP-FUCCI cells.



Determination of cell cycle- and endogenous autophagy-associated cellular accumulation of DiD-LIP

Next, we meticulously captured abundant CLSM images with intracellular co-localization of PIP-FUCCI and DiD fluorescence after a 2 h incubation of DiD-LIP using this platform (Supplementary Movies 1–8 and Supplementary Fig. 11). Subsequently, cell size, Total Fluorescence Intensity (TFI) and Mean Fluorescence Intensity (MFI) were respectively

calculated and analyzed at two-dimensional levels (Fig. 4, Table 1, Supplementary Fig. 12 and Supplementary Tables 6 and 7). Interestingly, our data showed that TFI (2D) of DiD-LIP across various cell cycle phases exhibited the same characteristics in both cell lines, which was $M < G1 \approx S < G2$. Further integration of the 3D reconstruction technique revealed the following characteristics of TFI (3D) of DiD-LIP: $M (\approx G1) < (G1 \approx) S < G2$ in WT PIP-FUCCI cells; $M < G1 < S < G2$ in ATG7 KO PIP-FUCCI cells.

Fig. 2 | Establishment of an alive and multi-functional technical platform for determining cell cycle- and autophagy-associated nanoparticle accumulation. **a** Schematic diagram shows the construction of cell lines stably expressing the PIP-FUCCI (cell cycle indicator) plasmid. Envelope plasmid PMD2.G, packing plasmid psPAX2 and transfer plasmid PIP-FUCCI were simultaneously added into 293 T cells. Afterwards, the culture medium was collected and concentrated, followed by application of lentiviral supernatant containing PIP-FUCCI to isogenic wild type (WT) and *ATG7* knockout (*ATG7* KO) U2OS cell lines. Subsequently, WT and *ATG7* KO PIP-FUCCI cell lines stably expressing PIP-FUCCI were obtained after selection with G418 and flow cytometry (FACS). **b** Schematic diagram indicates the establishment of a multi-functional platform for determining cell cycle phase- and autophagy-associated nanoparticle accumulation. WT and *ATG7* KO PIP-FUCCI cells were treated with DiD-labeled liposomes (DiD-LIP), at a dose equivalent to 5 µg/mL doxorubicin (DOX), or lipid nanoparticles (DiD-LNP), at a dose equivalent to 6 µg/mL nucleoside-modified mRNA (mRNA), for 2 h. The same volume of PBS was used

as a control. During the final 30 min of this incubation period, FITC-EpCAM (green fluorescence) was added to label the cell membrane. Complete distinguishment and collection of cells at four distinct cell cycle phases was achieved through combining PIP-FUCCI expression to indicate G1-phase (mVenus positive, green nucleus), S-phase (mCherry positive, red nucleus) and G2-phase (mVenus and mCherry double-positive, yellow nucleus) cells attached to the culture dish, with mitotic shake-off to collect detached or floating M-phase cells (mVenus and mCherry double-positive, yellow nucleus). Further integration of confocal laser scanning microscopy (CLSM) and three-dimensional reconstruction techniques enabled detection and calculation of nanoparticle accumulation at both two-dimensional and three-dimensional levels. **c** Representative light microscopic and CLSM images selected from 15 randomly chosen cells, demonstrating the successful construction and application of a technical platform using DiD-LIP (blue fluorescence) and WT PIP-FUCCI cells as a model system. Scale bars, 20 µm.

As expected, both cell lines exhibited a gradual increase in cell area (2D level) upon cell cycle progressing from G1 phase to G2 phase, followed by a decrease at M phase due to “mitotic rounding” to become spherical⁴⁴. Consistent with previous reports, cell volume (3D level) gradually increased while cells sequentially going through G1 phase, S phase, G2 phase and M phase of the cell cycle^{54,55}. Moreover, MFI (2D) based on cell area and MFI (3D) based on cell volume were initially calculated and analyzed. Impressively, MFI (2D) and MFI (3D) of DiD-LIP exhibited the same cell cycle-associated characteristics in both cell lines, which was $M < G1 \approx S \approx G2$ (Fig. 4, Table 1, Supplementary Fig. 12 and Supplementary Tables 6 and 7). These data may suggest that the relatively higher increase in cell size of G2-phase cells attenuated the aforementioned difference in TFI detected between G2 phase and G1 phase/S phase. It is noteworthy that generally, M-phase and G2-phase WT/*ATG7* KO PIP-FUCCI cells examined in suspension also respectively exhibited the lowest and highest DiD-LIP fluorescence intensities (or the minimum and maximum average fluorescence values) at both dimensional levels (Supplementary Fig. 13 and Supplementary Tables 8–10). These characteristics indicate that the influence of cell shape and culture status (adherent or floating upon detection) on fluorescence measurement with CLSM is trivial.

In a nutshell, our data have provided initial evidence that cells at the G2 phase and M phase, respectively, had the maximum and minimum nanoparticle accumulation. Interestingly, it has been suggested that M-phase cells have declined endocytosis and elevated cell membrane tension, which may assist the mother cell to prevent external disturbances during mitosis⁵⁶. These properties support our findings that M-phase cells had minimum nanoparticle accumulation among the four cell cycle phases, although the detailed mechanisms remain to be investigated further. Moreover, it is noteworthy that both TFI and MFI of DiD-LIP suggested an association between nanoparticle accumulation and endogenous autophagy. For instance, TFI (2D) of G1-phase and S-phase *ATG7* KO PIP-FUCCI cells, TFI (3D) of G1-phase and S-phase *ATG7* KO PIP-FUCCI cells, as well as MFI (2D) of M-phase *ATG7* KO PIP-FUCCI cells, all exhibited significant increases and surpassed those of WT PIP-FUCCI cells (Fig. 4, Supplementary Fig. 12 and Supplementary Tables 6 and 7).

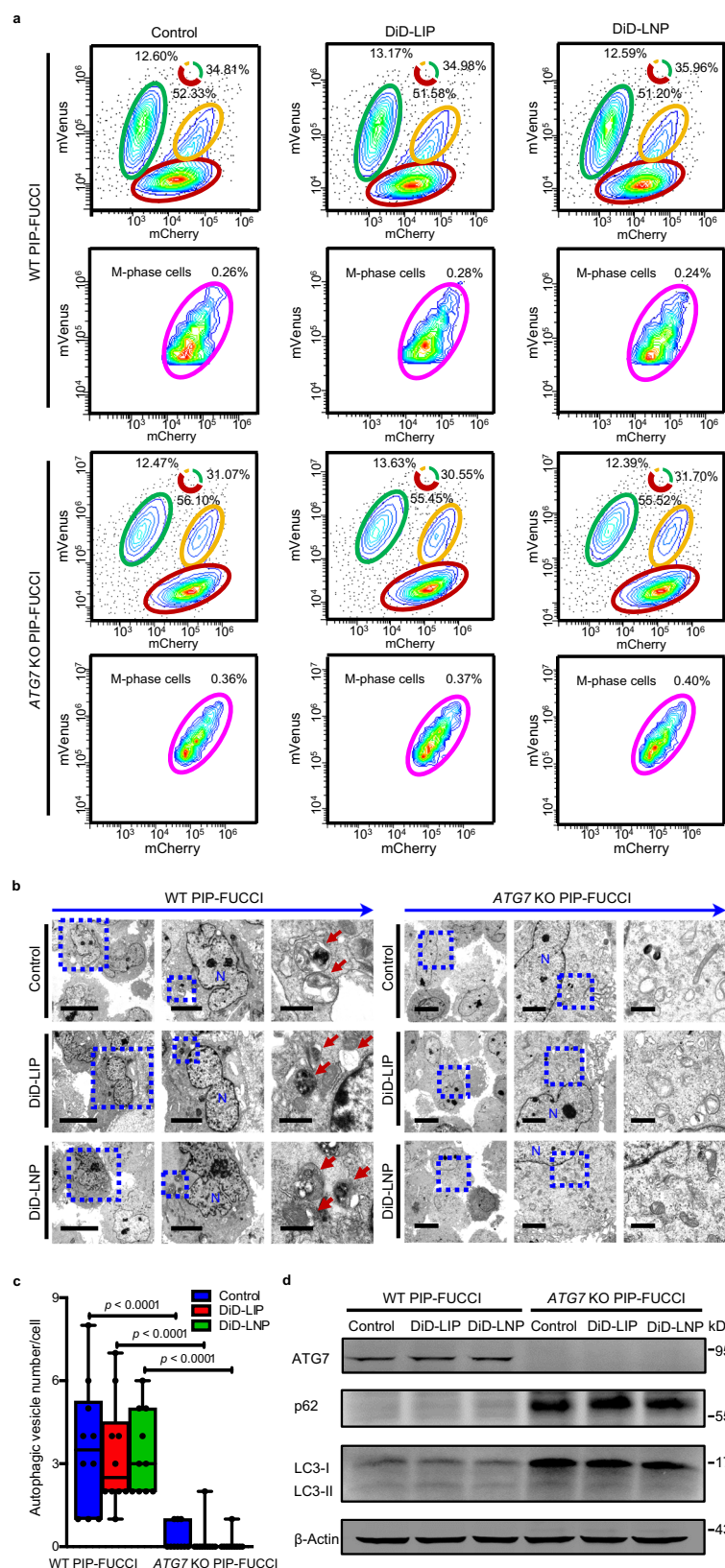
Determination of cell cycle- and endogenous autophagy-associated cellular accumulation of DiD-LNP

WT and *ATG7* KO PIP-FUCCI cells were further treated with DiD-LNP for 2 h, and the intracellular accumulation of DiD-LNP was evaluated with the multi-functional platform (Fig. 5, Table 1, Supplementary Movies 9–16, Supplementary Figs. 14 and 15 and Supplementary Tables 11 and 12). Impressively, TFI (2D) of DiD-LNP in both cell lines, and TFI (3D) and MFI (2D) of DiD-LNP in the WT PIP-FUCCI cell line, all exhibited the same cell cycle-associated characteristics as TFI (2D) of DiD-LIP, which was $M < G1 \approx S < G2$. MFI (3D) in WT and TFI (3D) in

ATG7 KO PIP-FUCCI cells showed similar characteristics, except $G1 < S$ in WT and $M \approx G1$ in *ATG7* KO PIP-FUCCI cells. Moreover, MFI (2D) and MFI (3D) in *ATG7* KO PIP-FUCCI cells were $M < G1 \approx S \approx G2$ and $M < (G1 \approx) S < (G1 \approx) G2$, respectively (Fig. 5, Table 1, Supplementary Fig. 15 and Supplementary Tables 11 and 12), coinciding with the aforementioned attenuation of differences between G2 phase and G1 phase/S phase due to relatively higher increase in cell size of G2-phase cells. The multi-dimensional data obtained with DiD-LNP confirmed that G2-phase cells had maximum, whereas M-phase cells had minimum nanoparticle accumulation. Interestingly, we noted that mean values of TFI and MFI of two model nanoparticles exhibited similar tendency in both cell lines, which is $M < G1 < S < G2$ (Figs. 4 and 5, Supplementary Figs. 12 and 15 and Supplementary Tables 6 and 11). These data might imply that when proliferating cells progress into a new cell cycle with physiological activities such as cellular protein and DNA synthesis gradually intensifying, nanoparticle accumulation becomes active in synchronization till the cells enter “torpid” M phase^{57–59}.

Moreover, it is noteworthy that M-phase cells have the minimum cell areas, which would weaken the difference of MFI (2D) between M-phase cells and cells at other phases. Nevertheless, M-phase cells of both cell lines still exhibited a significant decrease in MFI (2D) upon treatment with two model nanoparticles (nearly all $p < 0.0001$) (Figs. 4 and 5, Table 1, Supplementary Figs. 12 and 15, Supplementary Tables 6 and 7, 11 and 12). In contrast, M-phase cells have the maximum cell volumes, which would strengthen the difference of MFI (3D) between M-phase cells and cells at other phases. It is thereby logical that the following significant differences in MFI (3D) arose, although no difference was detected with corresponding TFI (3D): $M < G1$ in MFI (3D) of DiD-LIP in WT PIP-FUCCI cells, $M < G1$ and $M < S$ in MFI (3D) of DiD-LNP in *ATG7* KO PIP-FUCCI cells, all $p < 0.0001$ (Figs. 4 and 5, Table 1, Supplementary Figs. 12 and 15 and Supplementary Tables 6 and 7, 11 and 12).

Interestingly, different from DiD-LIP, that exhibited several significantly higher TFI and MFI in *ATG7* KO PIP-FUCCI cells than those in WT PIP-FUCCI cells, DiD-LNP showed increased TFI but reduced MFI in *ATG7* KO PIP-FUCCI cells compared with the WT strain. In detail, TFI (2D) of M-phase and TFI (3D) of G1-phase and M-phase *ATG7* KO PIP-FUCCI cells were significantly higher than those of WT PIP-FUCCI cells. However, both MFI (2D) and MFI (3D) of S-phase and G2-phase *ATG7* KO PIP-FUCCI cells were significantly lower than those in the WT strain (Fig. 5, Supplementary Fig. 15 and Supplementary Tables 11 and 12). These data indicate that autophagy might have diverse influences on cellular accumulation of nanoparticles, which deserves further investigation. Moreover, although cellular accumulation of DiD-LIP and DiD-LNP exhibited several common characteristics, varied features were also observed between these two nanoparticles regarding cell cycle- and autophagy-associated cellular



accumulation. These variations might attribute to different physicochemical properties between DiD-LIP and DiD-LNP, e.g., surface charge, nanoparticle composition and spatial structure, leading to distinctive “nano-bio” interactions such as different characteristics in endocytosis, subsequent endo-lysosomal escape, degradation and even exocytosis of nanoparticles.

Assessment of correlations between nanoparticle accumulation and cell size

Given that cell volumes gradually “grow” as the cell cycle progresses (Supplementary Tables 6 and 7, 11 and 12), we further evaluated whether increases in fluorescence intensity or nanoparticle accumulation correlate with increased cell size. Interestingly, correlation coefficient

Fig. 3 | Validation of cell cycle distribution and endogenous autophagy in WT and *ATG7* KO PIP-FUCCI cells with or without nanoparticle treatment.

a Representative flow cytometry data showing thorough cell cycle distribution selected from three independent biological replicates. Cells accumulated at G1 phase, S phase and G2 phase (upper panel for each cell line), as well as M phase (isolated with mitotic shake-off; lower panel for each cell line) were respectively circled in green, red, orange and purple, with corresponding percentages indicated. **b** Representative transmission electron microscope images of autophagic vesicles indicated by rust-red arrows. N, nucleus. Scale bars, from left to right, 10 μ m, 4 μ m and 1 μ m for WT PIP-FUCCI cells, and 10 μ m, 3 μ m and 1 μ m for *ATG7* KO PIP-FUCCI cells. **c** Statistical analyses of autophagic vesicle numbers per cell. Data were presented as median (IQR; $n = 10$ cells/group). Two-tailed Mann-Whitney

U tests with Monte Carlo approximation were used to compare autophagic vesicle number between WT and *ATG7* KO PIP-FUCCI cells within each group: Control ($U = 4.500$, $p < 0.0001$, 99% CI [0.000, 0.001], $r = 0.795$), DiD-LIP ($U = 3.000$, $p < 0.0001$, [0.000, 0.001], $r = 0.840$), DiD-LNP ($U = 0.000$, $p < 0.0001$, [0.000, 0.001], $r = 0.890$). The level of significance was set at $p < 0.05$. **d** Western blot analysis of autophagy-related proteins including ATG7, p62 and LC3. Cancer cells were respectively incubated with DiD-labeled liposomes (DiD-LIP, at a dose equivalent to 5 μ g/mL DOX) and lipid nanoparticles (DiD-LNP, at a dose equivalent to 6 μ g/mL mRNA) for 2 h. The same volume of PBS was used as a control. WT PIP-FUCCI, wild-type U2OS cells stably expressing PIP-FUCCI; *ATG7* KO PIP-FUCCI, *ATG7* knockout U2OS cells stably expressing PIP-FUCCI. Source data are provided as a Source Data file.

analyses between TFI (2D) and corresponding cell area revealed moderate ($r = 0.685$) and high ($r = 0.779$) correlations for DiD-LIP, and moderate ($r = 0.568$) and low ($r = 0.487$) correlations for DiD-LNP in WT and *ATG7* KO PIP-FUCCI cells, respectively (Fig. 6a). Moreover, two-tailed Fisher's z-test showed that the correlation coefficient for DiD-LIP was significantly higher than that for DiD-LNP in *ATG7* KO PIP-FUCCI cells. However, this characteristic was not observed in WT PIP-FUCCI cells (Supplementary Table 13).

Subsequently, correlation coefficients between TFI (2D) and cell area were carefully analyzed across four cell cycle phases. Our data showed that in DiD-LIP-treated WT PIP-FUCCI cells, high and very high correlations were respectively found for G1-phase ($r = 0.893$) and G2-phase ($r = 0.901$) cells, while moderate correlations were revealed for both S-phase ($r = 0.639$) and M-phase ($r = 0.563$) cells. In DiD-LIP-treated *ATG7* KO PIP-FUCCI cells, moderate correlations were observed for both G1-phase ($r = 0.531$) and S-phase ($r = 0.685$) cells, with a high correlation for G2-phase cells ($r = 0.783$) and no correlation was detected in M-phase cells (Supplementary Fig. 16). Meanwhile, in DiD-LNP-treated WT PIP-FUCCI cells, moderate correlations were found for both G1-phase ($r = 0.506$) and S-phase ($r = 0.682$) cells, with low correlations for both G2-phase ($r = 0.460$) and M-phase ($r = 0.482$) cells. In DiD-LNP-treated *ATG7* KO PIP-FUCCI cells, although no correlations were found for G1-phase, S-phase and M-phase cells, a moderate correlation was observed for G2-phase cells ($r = 0.553$) (Supplementary Fig. 17). Notably, further statistical analyses revealed that the correlation coefficients between TFI (2D) of DiD-LIP and cell area for S-phase and M-phase cells were significantly lower than those for G1-phase and G2-phase cells in the WT PIP-FUCCI cell line (Supplementary Table 14).

On the other hand, correlation coefficients between TFI (3D) and cell volume were analyzed in parallel. Our data showed that moderate ($r = 0.605$) and low ($r = 0.494$) correlations were respectively observed in DiD-LIP-treated WT and *ATG7* KO PIP-FUCCI cells, while a low ($r = 0.217$) and no correlation were observed for DiD-LNP-treated WT and *ATG7* KO PIP-FUCCI cells (Fig. 6b). Interestingly, consistent with the correlation coefficients between TFI (2D) and cell area, the higher correlation coefficient between TFI (3D) and cell volume was observed for DiD-LIP compared with DiD-LNP. Nevertheless, this characteristic was observed in WT but not *ATG7* KO PIP-FUCCI cells (Supplementary Table 15). Further analyses across cell cycle phases revealed high correlations for G1-phase ($r = 0.808$), G2-phase ($r = 0.860$) and M-phase ($r = 0.805$) DiD-LIP-treated WT PIP-FUCCI cells, with a low correlation for S-phase cells ($r = 0.493$). In DiD-LIP-treated *ATG7* KO PIP-FUCCI cells, a moderate correlation ($r = 0.648$) was found for G1-phase cells, with high correlations for S-phase ($r = 0.778$) and G2-phase ($r = 0.753$) cells and no correlation for M-phase cells (Supplementary Fig. 18). Meanwhile, in DiD-LNP-treated WT PIP-FUCCI cells, no correlation was found in G1-phase cells, while moderate correlations were observed for S-phase ($r = 0.518$), G2-phase ($r = 0.685$) and M-phase ($r = 0.700$) cells. In *ATG7* KO PIP-FUCCI cells, no correlations were found for G1-phase, S-phase and G2-phase cells, but a low correlation ($r = 0.428$) was observed for M-phase cells (Supplementary Fig. 19). Notably, further

statistical analyses confirmed that the correlation coefficient between TFI (3D) of DiD-LIP and cell volume for S-phase cells was significantly lower than those for G1-phase, G2-phase and M-phase cells in the WT PIP-FUCCI cell line (Supplementary Table 16). Taken together, these data demonstrate that cellular accumulation of nanoparticles is not directly or simply determined by cell size, but is affected by multiple factors such as cell cycle phase, cell line specificity and nanoparticle type.

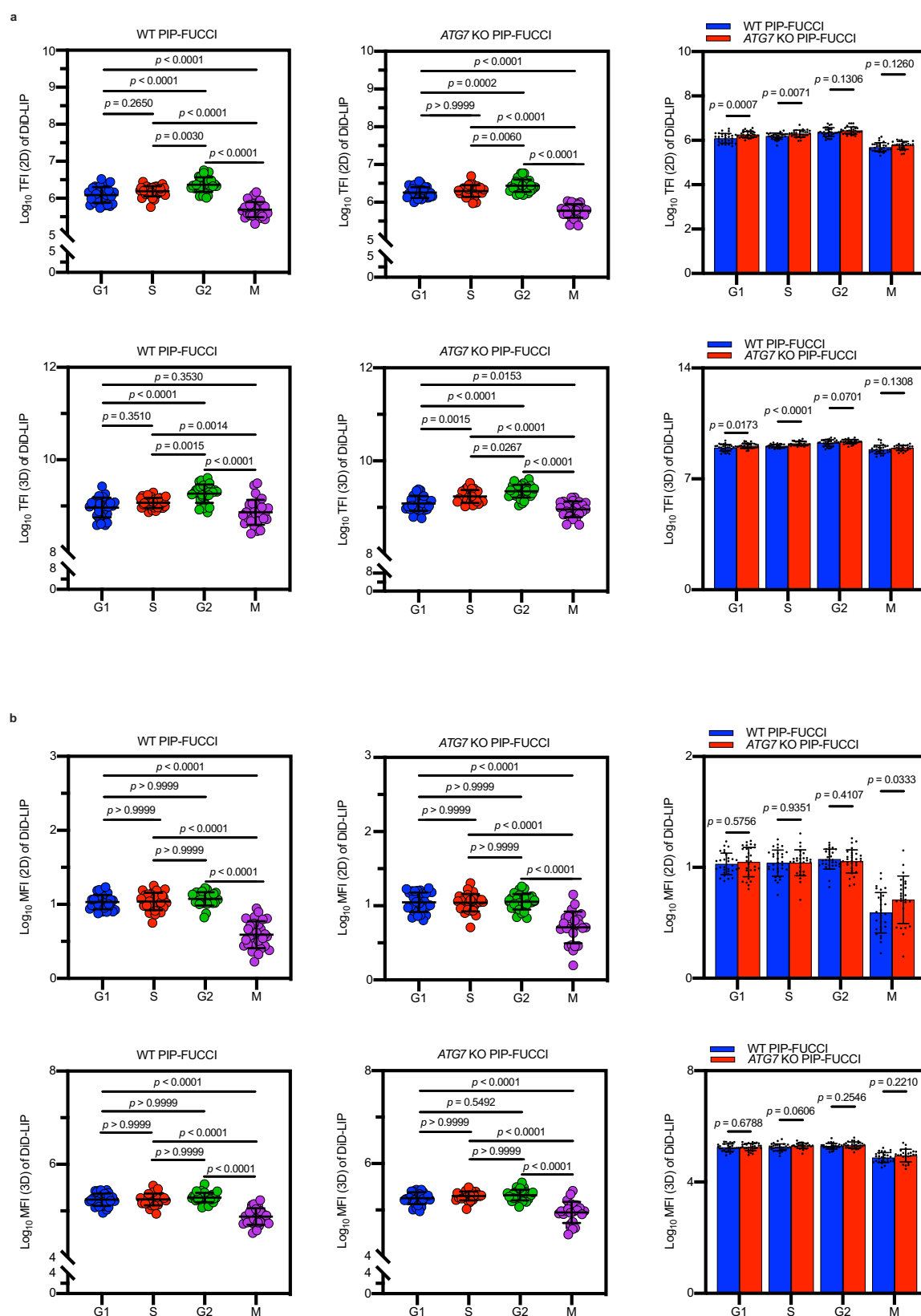
Assessment of correlations among fluorescence intensity-based parameters for determination of nanoparticle accumulation

Considering that TFI (2D), TFI (3D), MFI (2D) and MFI (3D) were used in combination for measuring nanoparticle accumulation, their potential correlations were assessed with two-tailed Spearman correlation analyses and Fisher's z-tests. As indicated in Table 2, when the correlations between two-dimensional levels were respectively evaluated for TFI and MFI in WT and *ATG7* KO PIP-FUCCI cell lines, moderate to very high correlations ($r = 0.689 - 0.932$) were obtained for all the assessed groups. Among them, moderate to high correlations ($r = 0.689 - 0.793$) were achieved for TFI and MFI of DiD-LIP, whereas high to very high correlations ($r = 0.811 - 0.932$) were detected for those of DiD-LNP. Further analyses revealed low to high correlations ($r = 0.495 - 0.711$) for TFI and corresponding MFI of DiD-LIP at the same dimensional level, while high to very high correlations ($r = 0.791 - 0.918$) for those of DiD-LNP ($r = 0.791$) (Table 3). Importantly, further two-tailed Fisher's z-tests discovered that correlation coefficients among TFI and MFI of DiD-LIP were significantly lower than those of DiD-LNP in WT and *ATG7* KO PIP-FUCCI cell lines (p -values, $0.0441 - < 0.0001$), except no correlation was detected between TFI (2D) and TFI (3D) of DiD-LIP with that of DiD-LNP in *ATG7* KO PIP-FUCCI cells ($p = 0.0860$) (Supplementary Table 17). These data indicate that correlations among TFI (2D), TFI (3D), MFI (2D) and MFI (3D), four fluorescence intensity-based parameters for measuring cellular accumulation of nanoparticles, might be affected by nanoparticle type or physicochemical characteristics of nanoparticles.

Interestingly, when comparing correlation coefficients among TFI and MFI in different cell lines, we found that the correlations between TFI (2D) and MFI (2D) of DiD-LNP in WT PIP-FUCCI cells were significantly higher than those in *ATG7* KO PIP-FUCCI cells (0.918 vs. 0.856 , $p = 0.0275$). Nevertheless, no other statistical differences were detected on the correlations among TFI and MFI between WT and *ATG7* KO PIP-FUCCI cell lines (Supplementary Table 18). These data suggest that, to a lesser extent than nanoparticle type, cell line-specific properties or the expression status of *ATG7* might affect the correlations among four fluorescence intensity-based parameters for the determination of nanoparticle accumulation.

Discussion

This study was initiated to develop and utilize a promising technical strategy for investigating the impacts of cell cycle and endogenous autophagy on cellular accumulation of biomedical nanoparticles. Our data demonstrate that several long-lasting methodological obstacles



were simultaneously overcome while mimicking physiological conditions to the maximum, through integrating multiple technical approaches, particularly *ATG7* KO, PIP-FUCCI transfection and mitotic shake-off, as well as 3D reconstruction. It is noteworthy that this “customizable” platform has offered a strategy for simultaneous

investigation on cell cycle and other “effectors” based on thorough cell cycle phase separation, e.g., parallel investigations on cell cycle and endogenous autophagy in the present study.

Impressively, by using this multi-functional, multi-dimensional and customizable platform, we presented initial evidence to

Fig. 4 | Determination of cell cycle- and endogenous autophagy-associated cellular accumulation of DiD-labeled liposomes (DiD-LIP) using the newly established technical platform. **a** Statistical analyses of Total Fluorescence Intensity (TFI) in G1-phase, S-phase, G2-phase and M-phase WT and *ATG7* KO PIP-FUCCI cells, respectively, measured at two-dimensional (2D, upper panel) and three-dimensional (3D, lower panel) levels. **b** Statistical analyses of Mean Fluorescence Intensity (MFI) in WT and *ATG7* KO PIP-FUCCI cells, respectively, measured at the aforementioned four cell cycle phases, as well as at 2D (upper panel) and 3D (lower panel) levels. Cancer cells were incubated with DiD-LIP at a dose equivalent to 5 µg/mL DOX for 2 h. The same volume of PBS was used as a control. All data were

log₁₀-transformed and presented as mean ± SD (WT PIP-FUCCI, *n* = 30, 30, 30, 29; *ATG7* KO PIP-FUCCI, *n* = 30, 28, 30, 25 cells for G1 phase, S phase, G2 phase, and M phase, respectively). Statistical analyses of DiD-LIP accumulation among four distinct cell cycle phases were conducted using one-way ANOVA followed by Bonferroni multiple comparisons test, while differences between WT and *ATG7* KO PIP-FUCCI cell lines were evaluated with two-tailed independent sample *t*-tests (complete statistical results provided in Supplementary Table 7). The level of significance was set at *p* < 0.05. WT PIP-FUCCI, wild-type U2OS cells stably expressing PIP-FUCCI; *ATG7* KO PIP-FUCCI, *ATG7* knockout U2OS cells stably expressing PIP-FUCCI. Source data are provided as a Source Data file.

Table 1 | Cell cycle- and autophagy-associated accumulation patterns of DiD-LIP and DiD-LNP by cancer cells based on the multi-functional platform

Cell line	Dimension	DiD-LIP		DiD-LNP	
		TFI (a.u.)	MFI (a.u.)	TFI (a.u.)	MFI (a.u.)
WT PIP-FUCCI	2D	M < G1 ≈ S < G2	M < G1 ≈ S ≈ G2	M < G1 ≈ S < G2	M < G1 ≈ S < G2
WT PIP-FUCCI	3D	M (≈ G1) < (G1 ≈) S < G2	M < G1 ≈ S ≈ G2	M < G1 ≈ S < G2	M < G1 < S < G2
<i>ATG7</i> KO PIP-FUCCI	2D	M < G1 ≈ S < G2	M < G1 ≈ S ≈ G2	M < G1 ≈ S < G2	M < G1 ≈ S ≈ G2
<i>ATG7</i> KO PIP-FUCCI	3D	M < G1 < S < G2	M < G1 ≈ S ≈ G2	M ≈ G1 ≈ S < G2	M < (G1 ≈) S < (G1 ≈) G2

TFI and MFI were log₁₀-transformed. Statistical analyses among four distinct cell cycle phases were conducted using one-way ANOVA, followed by a Bonferroni multiple comparisons test. ≈, no significant difference, TFI total fluorescence intensity, MFI mean fluorescence intensity, 2D two-dimensional level, 3D three-dimensional level. Source data are provided as a Source Data file.

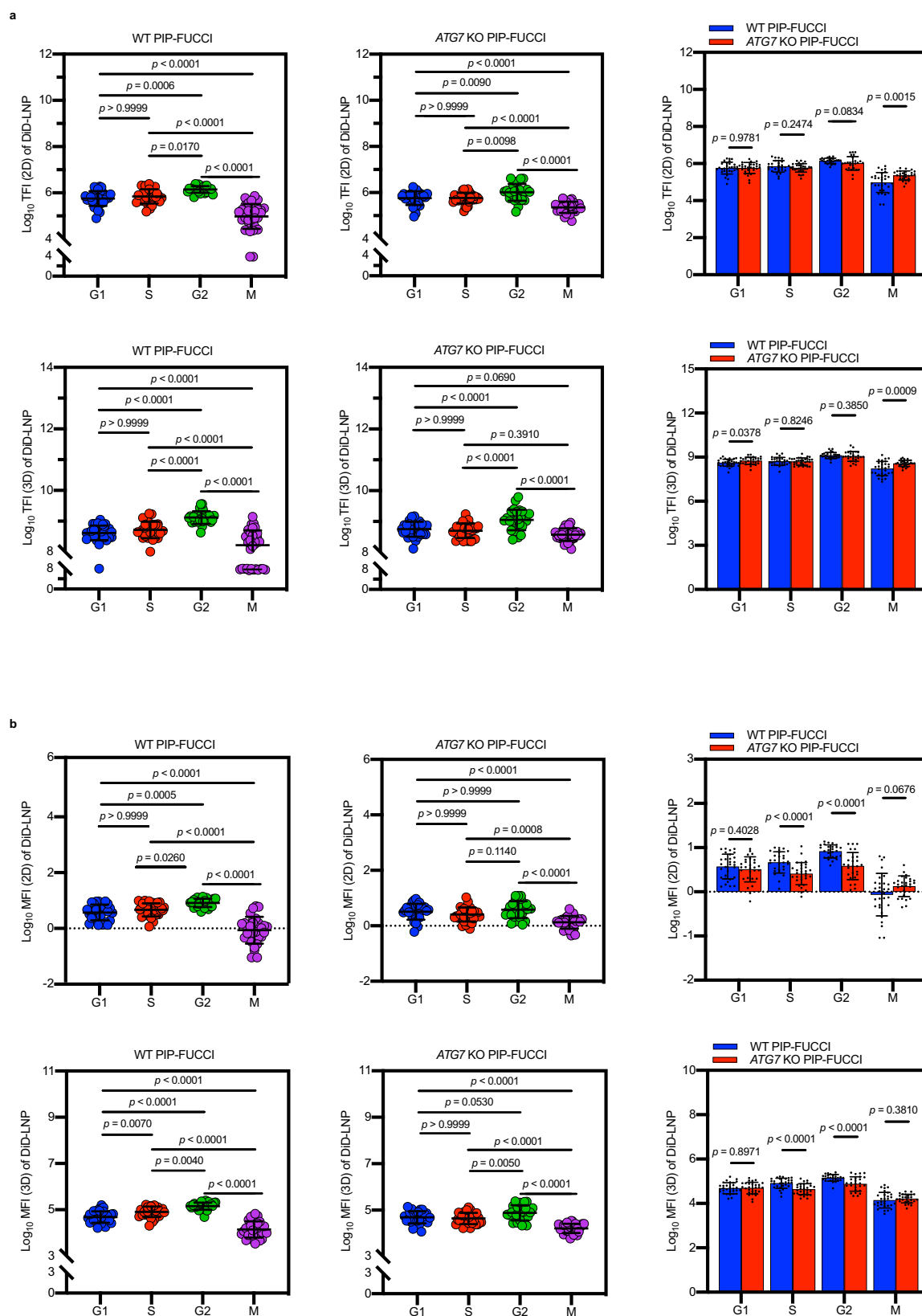
demonstrate that after a 2 h incubation of DiD-LIP and DiD-LNP, G2-phase and M-phase cancer cells respectively possessed the maximum and minimum nanoparticle accumulations (Figs. 4 and 5, Table 1, Supplementary Figs. 12 and 15 and Supplementary Tables 6 and 7, 11 and 12). These findings are of particular importance as these two distinct cell populations were muddled up together (so called G2/M-phase cells) in previous literatures due to technical limitations in distinguishing one population from another under physiological conditions^{11–22}. Interestingly, cell cycle-associated nanoparticle accumulation was observed not only between spherical M-phase and adherent G2-phase cells, but among adherent G1-phase, S-phase and G2-phase WT and *ATG7* KO PIP-FUCCI cells. In general, mean values of TFI and MFI of both DiD-LIP and DiD-LNP exhibited similar cell cycle-associated tendencies in WT and *ATG7* KO PIP-FUCCI cells, which was M < G1 < S < G2 (Figs. 4 and 5, Table 1, Supplementary Figs. 12 and 15 and Supplementary Tables 6 and 7, 11 and 12). These data may suggest a synchronization in intensified cellular metabolism and enhanced nanoparticle accumulation while the cell cycle progressing from G1 phase to G2 phase^{57–59}. Nevertheless, detailed mechanisms mediating cell cycle-associated nanoparticle accumulation warrant further exploration, particularly for “torpid” M-phase cells. Moreover, although cell sizes gradually increased while cell cycle progressing, intensive analyses on obtained data revealed that cellular accumulation of nanoparticles is associated with multiple factors including cell cycle phase, cell line-specific properties/*ATG7* status and nanoparticle type, rather than directly or simply determined by cell sizes (Fig. 6, Supplementary Figs. 16–19 and Supplementary Tables 13–16).

Until now, there have been four reports that have explored the influence of autophagy on cellular accumulation of nanoparticles, including C6-tagged Ag nanoparticles³⁰, NIR-labeled carboxylated polystyrene nanoparticles^{31,32}, and hyaluronic acid-modified MIL-125³³, all of which used 2D-based fluorescence intensity for accumulation assessment and non-specific autophagy inhibitors for autophagy blockade. Although multiple factors such as nanoparticle type and cell line-specific properties might be associated with previous controversial findings on autophagy-associated nanoparticle accumulation, it is notable that different from *ATG7* knockout, that specifically blocks endogenous autophagy, non-specific autophagy inhibitors possess non-autophagy-related pharmacological effects, including

induction of cell death and lysosomotropic activities. Therefore, non-specific autophagy inhibitors may have “side effects” that interfere with the cellular accumulation of nanoparticles^{34,35}. Interestingly, our data generally suggest that *ATG7* knockout enhanced nanoparticle accumulation, as demonstrated by TFI/MFI of DiD-LIP and TFI of DiD-LNP (Figs. 4 and 5, Supplementary Figs. 12 and 15 and Supplementary Tables 6 and 7). Although further verifications are needed, our findings have provided a novel line of supportive evidence for combined use of anticancer modalities with autophagy blockers, which is currently under preclinical and clinical evaluations^{60–62}.

Herein, TFI (2D), TFI (3D), MFI (2D) and MFI (3D) were firstly used in combination for measuring cellular accumulation of fluorescence-labeled nanoparticles to improve our understanding on “cell-nano” interactions. Interestingly, positive correlations were detected among these parameters, albeit with varied correlation coefficients, possibly due to nanoparticle type (LIP or LNP) and cell line specificity/*ATG7* status (Tables 2 and 3 and Supplementary Tables 17 and 18). Nevertheless, assessing nanoparticle accumulation at the 3D level involves z-stack scanning and 3D reconstruction, they may offer more comprehensive considerations of related factors, such as cell shape and cell size disparities^{54,55} and non-uniform intracellular distribution of nanoparticles. In other words, parameters based on the 3D level might aid in mitigating the constraints associated with the 2D level and facilitate “data correction”. Therefore, when cells have significant morphological heterogeneity while precise results are expected, data analyses at the 3D level would be superior to 2D level. Moreover, if cells and nanoparticles are respectively considered as individuals and therapeutic drugs, these fluorescence intensity-based parameters remind us of “similar” parameters used in clinics, including total and mean body surface area (BSA), total body weight (TBW), body mass index (BMI), as well as drug dose-related parameters⁶³. Further application and assessment of these parameters will not only deepen our understandings on their values, but promote the optimization of the technical platform.

In brief, although several important issues warrant additional research, e.g., detailed mechanisms mediating cell cycle- and autophagy-associated nanoparticle accumulation, possible interplay between cell cycle and autophagy, merits of TFI and MFI at different dimensional levels, and potential nanoparticle- and cell line-mediated specificities on nanoparticle accumulation, our findings may open new



insights into optimizing the design and application of lipid-based and possibly other nanomedicines besides providing a valuable technical solution. Particularly, around 3,200 LIP/LNP-based nano-formulations are currently under clinical investigations (<http://www.chinadrugtrials.org.cn/index.html>, <https://www.who.int/clinical-trials-registry-platform>, <https://clinicaltrials.gov/>).

Methods

Major reagents

Cholesterol, 1-palmitoyl-2-stearoyl-sn-glycero-3-phosphocholine (HSPC), 1,2-distearoyl-sn-glycero-3-phosphocholine (DSPC) and 1,2-distearoyl-sn-glycero-3-phosphoethanolamine-N-[methoxy-(polyethylene glycol)-2000] (mPEG₂₀₀₀-DSPE) were purchased from

Fig. 5 | Determination of cell cycle- and endogenous autophagy-associated cellular accumulation of DiD-labeled lipid nanoparticles (DiD-LNP) using the newly established technical platform. **a** Statistical analyses of Total Fluorescence Intensity (TFI) in G1-phase, S-phase, G2-phase and M-phase WT and *ATG7* KO PIP-FUCCI cells, respectively, measured at two-dimensional (2D, upper panel) and three-dimensional (3D, lower panel) levels. **b** Statistical analyses of Mean Fluorescence Intensity (MFI) in WT and *ATG7* KO PIP-FUCCI cells, respectively, measured at four distinct cell cycle phases, as well as at 2D (upper panel) and 3D (lower panel) levels. Cancer cells were incubated with DiD-LNP at a dose equivalent to 6 $\mu\text{g}/\text{mL}$ mRNA for 2 h. The same volume of PBS was used as a control. All data were \log_{10} -

transformed and presented as mean \pm SD (WT PIP-FUCCI: $n = 30, 28, 26, 30$; *ATG7* KO PIP-FUCCI: $n = 28, 30, 26, 27$ cells for G1 phase, S phase, G2 phase, and M phase, respectively). Statistical analyses of DiD-LNP accumulation among four distinct cell cycle phases were conducted using one-way ANOVA followed by Bonferroni multiple comparisons test, while differences between WT and *ATG7* KO PIP-FUCCI cell lines were evaluated with two-tailed independent sample *t*-tests (complete statistical results provided in Supplementary Table 12). The level of significance was set at $p < 0.05$. WT PIP-FUCCI, wild-type U2OS cells stably expressing PIP-FUCCI; *ATG7* KO PIP-FUCCI, *ATG7* knockout U2OS cells stably expressing PIP-FUCCI. Source data are provided as a Source Data file.

Lipoid GmbH (Ludwigshafen, Germany). [(4-Hydroxybutyl)azanediyl] di(hexane-6,1-diyl) bis(2-hexyldecanoate) (ALC-0315) and 2-[(polyethylene glycol)-2000]-N,N-ditetradecylacetamide (ALC-0159) were acquired from SINOPEG (Xiamen, China). 1,1'-Dioctadecyl-3,3',3'-tetramethylindotricarbocyanine, 4-chlorobenzenesulfonate salt (DiD) was from MKBio (Shanghai, China). Firefly luciferase mRNA (LUC mRNA) was from Afana Biotechnology (Hefei, China). Ferric chloride hexahydrate and ammonium thiocyanate were from Sigma-Aldrich (St. Louis, MO, USA). Lipofectamine 3000, Opti-MEM, Trypsin-EDTA (0.05%), protein marker and Hoechst33342 solution were purchased from Thermo Fisher Scientific (Waltham, MA, USA). Polybrene was from Santa Cruz (Dallas, TX, USA). G418 was from InvivoGen (San Diego, CA, USA). Glutaraldehyde, ethanol and acetone were from Hushi Chemical (Shanghai, China). Lead citrate was from Macklin (Shanghai, China). RIPA buffer and DAPI staining solution were from Beyotime (Shanghai, China). Protease inhibitor and phosphatase inhibitor were from Yeason (Shanghai, China).

Lentivirus concentration kit (Cat. NO. 41101ESS0) was acquired from Yeason. BCA protein assay kit (Cat. NO. FD2001) was obtained from Thermo Fisher Scientific. E.Z.N.A. Endo-free plasmid maxi kit (Cat. NO. D6926-03) was from Omega (Norcross, GA, USA). Plasmids of psPAX2 (Cat. NO. 12260), pMD2.G (Cat. NO. 12259), pLenti-PGK-Neo-PIP-FUCCI (PIP-FUCCI) (Cat. NO. 118616) and pLenti PGK Neo DEST (empty vector) (Cat. NO. 19067) were from Addgene (Cambridge, MA, USA).

Anti-ATG7 antibody (Cat. NO. ab133528; clone name, EPR6251) and anti-SQSTM1/p62 antibody (Cat. NO. ab91526) were from Abcam (Waltham, MA, USA). LC3A/B XP Rabbit mAb (Cat. NO. 12741S; clone name, D3U4C) and β -actin antibody (Cat. NO. 4967) were from Cell Signaling Technology (Danvers, MA, USA). EpCAM monoclonal antibody, FITC (Cat. NO. MA1-10197; clone name, VU-ID9), goat anti-rabbit IgG (H+L) highly cross-adsorbed secondary antibody (Alexa Fluor 488) (Cat. NO. A32731), goat anti-rabbit IgG (H+L) cross-adsorbed secondary antibody (Alexa Fluor 546) (Cat. NO. A11010), and goat anti-mouse IgG (H+L) cross-adsorbed secondary antibody (Alexa Fluor 546) (Cat. NO. A11003) were from Thermo Fisher Scientific.

Cell lines and cell cultures

Wild type (WT) and *ATG7* knockout (*ATG7* KO) human osteosarcoma cancer cell lines U2OS were kind gifts from Professor Qiming Sun at Zhejiang University School of Medicine. Human kidney epithelial cell line 293 T was from the Shanghai Institute of Cells, Chinese Academy of Sciences. All cell lines, including newly established WT and *ATG7* KO PIP-FUCCI cell lines, were authenticated by STR profiling (Tsingke Biotechnology, Beijing, China) and confirmed to be mycoplasma-free. All cell lines were in cultured in DMEM supplemented with 10% (v/v) fetal bovine serum and maintained at 37 °C in an atmosphere containing 5% CO₂.

Preparation of model nanoparticles DiD-LIP and DiD-LNP

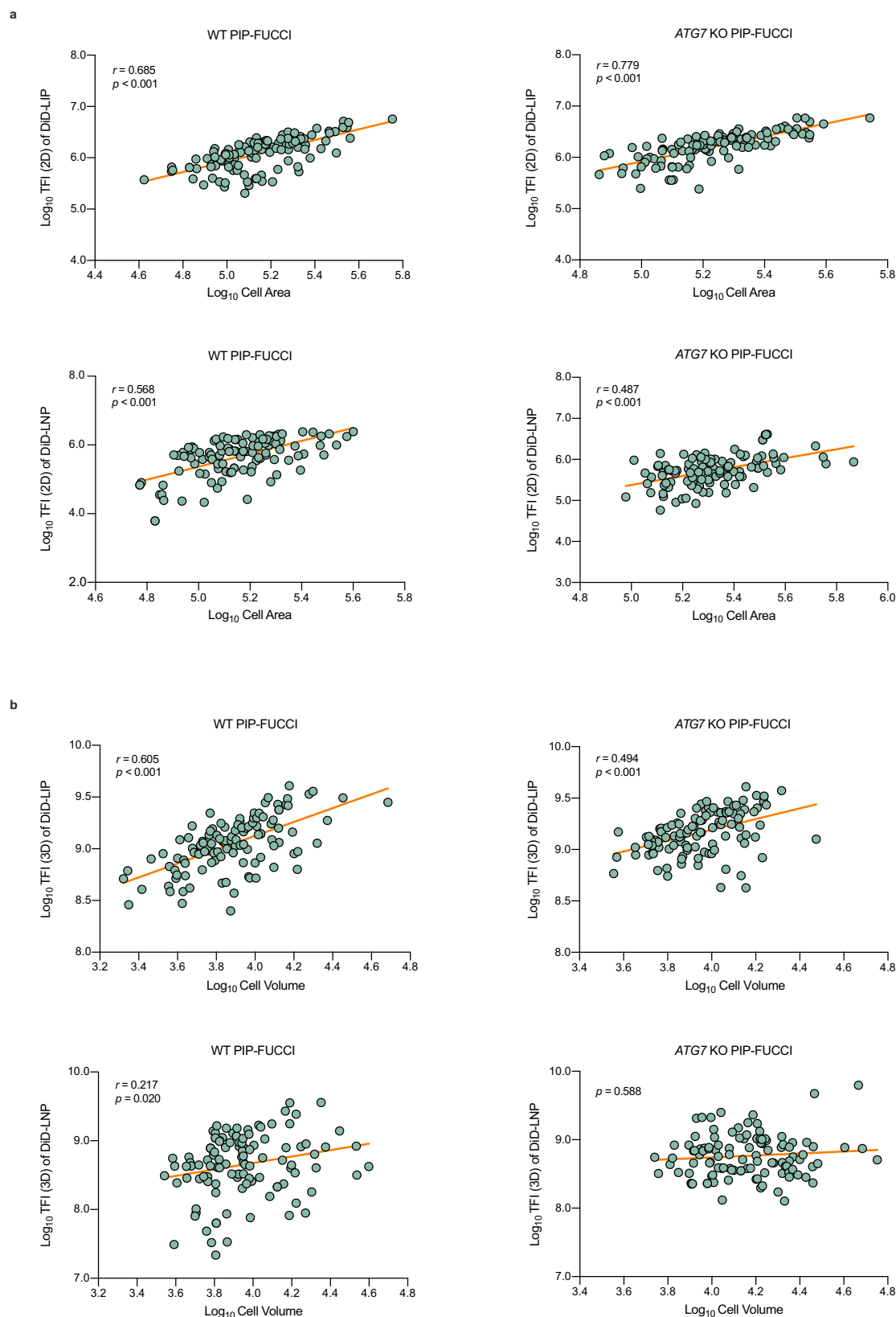
DiD-LIP was synthesized according to the officially published formulation of Doxil[®]³⁸, and previous reports⁶⁴. First, HSPC, cholesterol and mPEG₂₀₀₀-DSPE, at 56.6:38.1:5.3 molar ratio, were hydrated in

10 mM sucrose-histidine buffer at pH6.5. Subsequently, DiD was added into the lipid mixture at a concentration of 0.4 mol%, followed by vortex at 60 °C for 3 min to generate multilamellar vesicles (MLVs). Finally, the MLVs were reduced in size using 400, 100, 80, and 50 nm-pore size polycarbonate filters with a 10-mL extruder barrel (Northern Lipids, Vancouver, Canada), and stored at a temperature of 4 °C until use.

DiD-LNP was prepared based on the officially published formulation of Comirnaty[®]³⁹. using a modified procedure we previously described^{4,65}. Initially, ALC-0315, DSPC, cholesterol and ALC-0159 were dissolved at a molar ratio of 46.3: 9.4: 42.7: 1.6 to fabricate the ethanol phase and DiD was then added into the lipids at a concentration of 0.4 mol%. Meanwhile, LUC mRNA was dissolved in 20 mM citrate buffer to prepare the aqueous phase. Subsequently, the above two phases were mixed with a microfluidic mixer (Precision Nanosystems, Canada) at a flow rate ratio of 1:3 (ethanol:aqueous). Following this, the resulting nanoparticle solution was subjected to dialysis against 10 \times volume of PBS for at least 18 h using tangential flow filtration (TFF) membranes with molecular weight cut-offs of 100 kD (Sartorius Stedim, Germany). With the assistance of an Amicon ultracentrifugal filter (EMD Millipore, Billerica, MA, USA), the nanoparticle solution was passed through a 0.22 μm filter and ultimately concentrated to the desired concentration.

General characterization of DiD-LIP and DiD-LNP

A Zetasizer Nano ZS instrument (Malvern Instruments Ltd, Malvern, UK) was employed to measure the hydrodynamic size (Z-average), polydispersity index (PDI) and zeta potential of DiD-LIP and DiD-LNP diluted 1:100 in PBS at 25 °C⁴. To evaluate their stability in an experimental environment, DiD-LIP and DiD-LNP were diluted 1:100 in culture medium and incubated at 37 °C. Aliquots were collected at 1, 2, 6, 12 and 24 h for Z-average and PDI measurements at 37 °C. Three independent biological replicates were performed. Furthermore, the morphology of DiD-LIP and DiD-LNP was examined by Cryo-TEM using a Talos F200C instrument (FEI/Thermo Fisher Scientific) equipped with a Ceta 4 k \times 4 k camera at 200 kV acceleration voltage, with 15 randomly selected fields imaged. In addition, phospholipid concentrations (HSPC and mPEG₂₀₀₀-DSPE for DiD-LIP; DSPC for DiD-LNP) were quantified through Steward's assay^{4,66,67}. Briefly, 10 μL of the lipid sample was mixed with 990 μL of chloroform, followed by the addition of 1 mL ammonium ferriethiocyanate reagent. After vortexing and centrifugation (300 \times g, 15 min), absorbance was measured at 470 nm using a UV500 spectrophotometer (Thermo Fisher Scientific). Calibration curves (DSPC: 25 - 200 $\mu\text{g}/\text{mL}$; HSPC: 25 - 150 $\mu\text{g}/\text{mL}$) were applied to determine the phospholipid concentrations of DiD-LIP and DiD-LNP. According to previous pharmacokinetics studies and related literatures, the doses of DiD-LIP and DiD-LNP used in this study were equivalent to 5 $\mu\text{g}/\text{mL}$ DOX^{38,68,69} (42.67 $\mu\text{g}/\text{mL}$ of lipids including 25.61 $\mu\text{g}/\text{mL}$ of HSPC, 8.53 $\mu\text{g}/\text{mL}$ of mPEG₂₀₀₀-DSPE and 8.53 $\mu\text{g}/\text{mL}$ of Cholesterol) and 6 $\mu\text{g}/\text{mL}$ mRNA⁷⁰⁻⁷² (154.20 $\mu\text{g}/\text{mL}$ of lipids including 85.80 $\mu\text{g}/\text{mL}$ of ALC-0315, 10.20 $\mu\text{g}/\text{mL}$ of ALC-0159, 18.00 $\mu\text{g}/\text{mL}$ of DSPC and 40.20 $\mu\text{g}/\text{mL}$ of Cholesterol), respectively. The same volume of PBS was used as a control.



Construction of isogenic WT and ATG7 KO PIP-FUCCI cell lines stably expressing cell cycle-indicating PIP-FUCCI plasmid

The cell cycle-indicating PIP-FUCCI plasmid encodes mVenus fused to the PIP degen (*Cdt1₁₋₁₇*),

which is rapidly degraded at the onset of DNA replication, and mCherry fused to *Geminin* (*Gem1-110*), which accumulates during S/G2/M phases and is degraded at late M phase^{36,73}. In U2OS cells transfected with PIP-FUCCI, G1-phase (mVenus single-positive) cells show green

Fig. 6 | Assessment of correlations between nanoparticle accumulation and cell size. **a** Two-tailed Spearman correlation analyses showing the correlations between Total Fluorescence Intensity (TFI) and cell area for DiD-LIP (upper panel) and DiD-LNP (lower panel) in WT and *ATG7* KO PIP-FUCCI cells at the two-dimensional (2D) level. For DiD-LIP: WT PIP-FUCCI ($r = 0.685$, $p < 0.001$, 95% CI [0.577, 0.775]); *ATG7* KO PIP-FUCCI ($r = 0.779$, $p < 0.001$, [0.693, 0.844]). For DiD-LNP: WT PIP-FUCCI ($r = 0.568$, $p < 0.001$, [0.422, 0.687]); *ATG7* KO PIP-FUCCI ($r = 0.487$, $p < 0.001$, [0.328, 0.628]). **b** Two-tailed Spearman correlation analyses showing the correlations between Total Fluorescence Intensity (TFI) and cell volume for DiD-LIP (upper panel) and DiD-LNP (lower panel) in WT and *ATG7* KO PIP-FUCCI cells at the three-dimensional (3D) level. For DiD-LIP: WT PIP-FUCCI ($r = 0.605$, $p < 0.001$, [0.450, 0.728]); *ATG7* KO PIP-FUCCI ($r = 0.494$, $p < 0.001$,

[0.326, 0.646]). For DiD-LNP: WT PIP-FUCCI ($r = 0.217$, $p = 0.020$, [0.032, 0.394]); *ATG7* KO PIP-FUCCI ($r = 0.053$, $p = 0.588$, [-0.128, 0.234]). Cancer cells were respectively, incubated with DiD-labeled liposomes (DiD-LIP, at a dose equivalent to 5 $\mu\text{g/mL}$ DOX) and lipid nanoparticles (DiD-LNP, at a dose equivalent to 6 $\mu\text{g/mL}$ mRNA) for 2 h. The same volume of PBS was used as a control. All data were \log_{10} -transformed ($n = 119$, 113 cells for WT and *ATG7* KO PIP-FUCCI treated with DiD-LIP; $n = 114$, 111 cells for WT and *ATG7* KO PIP-FUCCI treated with DiD-LNP, respectively). The level of significance was set at $p < 0.05$, and the correlation strengths were determined using correlation coefficients (r). WT PIP-FUCCI, wild-type U2OS cells stably expressing PIP-FUCCI; *ATG7* KO PIP-FUCCI, *ATG7* knockout U2OS cells stably expressing PIP-FUCCI. Source data are provided as a Source Data file.

nuclear fluorescence, S-phase (mCherry single-positive) cells exhibit red nuclear fluorescence, while G2/M-phase (mVenus and mCherry double-positive) cells display yellow (overlap of green and red) nuclear fluorescence³⁶.

WT and *ATG7* KO U2OS cell lines stably expressing PIP-FUCCI were generated as follows. 293 T cells (1×10^6 cells per 10-cm dish) were co-transfected with PIP-FUCCI, psPAX2 and pMD2.G plasmids using Lipofectamine 3000, with empty vector serving as a negative control. The medium was replaced after 8 h, and lentiviral supernatant was collected at 72 h post-transfection. WT and *ATG7* KO U2OS cells were seeded at 6×10^4 cells per well in 6-well plates and cultured overnight, then transduced with concentrated lentivirus in the presence of 8 $\mu\text{g/mL}$ polybrene. After G418 selection (500 $\mu\text{g/mL}$, 7 days), PIP-FUCCI-expressing cells were sorted by FACSaria II flow cytometer (BD Biosciences, San Jose, CA, USA) based on strong mVenus and/or mCherry fluorescence, with empty vector-transfected cells served as controls.

Evaluation of the influence of PIP-FUCCI transfection on cell morphology and proliferation

Morphology was assessed in 15 randomly selected fields for each cell line (WT/*ATG7* KO Vector and WT/*ATG7* KO PIP-FUCCI) using a light microscope. For proliferation assays, cells were seeded at 1×10^5 cells per well in 6-well plates and counted every 24 h for 120 h with a Countess II FL Automated Cell Counter (Thermo Fisher Scientific). Three independent biological replicates were performed. Doubling time (T , hours) was calculated using the following equation:

$$T = t \times \log_{10}(2) / [\log_{10}(N_f) - \log_{10}(N_i)] \quad (1)$$

where t is the culture duration (hours), N_f is the final cell number, and N_i is the initial cell number.

Cell cycle tracking in WT and *ATG7* KO PIP-FUCCI cells via time-lapse live-cell imaging

WT and *ATG7* KO PIP-FUCCI cells were seeded at 8×10^4 cells per confocal dish and incubated overnight. Live-cell imaging was performed using an Andor BC43 spinning disk confocal microscope (Oxford Instruments, Abingdon, UK) at $20 \times$ magnification (NA 0.8). 20 random fields were monitored for up to 25 h, corresponding to the estimated cell doubling time (Supplementary Fig. 5). Filter sets were as follows: mVenus (excitation: 514 nm, emission: 519–590 nm) and mCherry (excitation: 561 nm, emission: 570–620 nm). Images were acquired every 5 min under controlled conditions (5% CO_2 , 37 °C), and analyzed with Imaris 9.6.1 (Bitplane, Zurich, Switzerland).

DNA content analysis in WT and *ATG7* KO PIP-FUCCI cells by flow cytometry

WT and *ATG7* KO PIP-FUCCI cells were seeded at 1.5×10^6 cells per T175 flask and cultured overnight. M-phase cells were collected by gentle shaking (a method designated as mitotic shake-off³⁷), based on their distinct spherical shape and decreased adhesion capability⁴⁴, whereas adherent G1-phase, S-phase and G2-phase cells were harvested by

trypsinization. Each cell sample was rinsed three times with PBS, stained with 1 mL of Hoechst33342 solution (10 $\mu\text{g/mL}$, 30 min, 37 °C), and analyzed on a CytoFLEX LX flow cytometer (Beckman Colter, Indianapolis, IN, USA). Hoechst33342, mVenus and mCherry fluorescence were excited using 375 nm, 488 nm and 561 nm lasers, respectively, and detected with 450/45 nm, 525/40 nm and 610/20 nm bandpass filters. Three independent biological replicates were performed. The correspondence between fluorescence and DNA content was as follows: adherent G1-phase cells (mVenus positive) with 2 N DNA content; adherent S-phase cells (mCherry positive) with DNA content ranging from 2 N to 4 N DNA content; and adherent G2-phase and floating M-phase cells (mVenus and mCherry double-positive) with 4 N DNA content. Data were analyzed with FlowJo 10.5.3 (Tree Star, Ashland, OR, USA).

Evaluation of possible effects of nanoparticles on cell cycle distribution with flow cytometry

WT and *ATG7* KO PIP-FUCCI cells were seeded at 1×10^6 cells per 10-cm dish and cultured overnight. The cells were then respectively, incubated with DiD-LIP and DiD-LNP for 2 h. M-phase cells were collected by mitotic shake-off³⁷, while adherent G1-phase, S-phase and G2-phase cells were harvested by trypsinization. In addition, WT and *ATG7* KO PIP-FUCCI cells (3×10^5 cells per well in 6-well plates) were respectively incubated with PBS, DiD-LIP and DiD-LNP for 12, 24 and 48 h. Cells were routinely harvested by trypsinization. All samples were rinsed three times with PBS, stained with 1 mL of DAPI, and analyzed in equal volumes with a CytoFLEX LX flow cytometer (Beckman Colter). DAPI, mVenus and mCherry channels were respectively, excited with 375, 488 and 561 nm lasers, and detected with corresponding 450/45, 525/40 and 610/20 nm bandpass filters. Cells exhibited the following fluorescence: G1 phase (mVenus positive), green fluorescence; S phase (mCherry positive), red fluorescence; G2 phase and M phase (mVenus and mCherry double-positive), yellow fluorescence. Three independent biological replicates were performed. Data were analyzed with FlowJo 10.5.3 (Tree Star) using the gating strategy as shown in Supplementary Fig. 20.

Examination of possible effects of nanoparticles on autophagic vesicle formation with TEM

WT and *ATG7* KO PIP-FUCCI cells were seeded at 7×10^5 cells per 6-cm dish and cultured overnight. The cells were then, respectively, incubated with DiD-LIP and DiD-LNP for 2 h. After treatment, cells were fixed overnight with 2.5% glutaraldehyde at 4 °C and washed three times with PBS for 10 min each. Post-fixation was performed with 1% osmium tetroxide for 1 h, followed by PBS rinsing and staining with 2% uranyl acetate for 30 min. Dehydration was carried out using a graded ethanol series at 50, 70, 90 and 100%, each for 15 min, followed by two changes of 100% acetone for 20 min each. Ultrathin sections were prepared using a Leica UC7 microtome (Leica, Solms, Germany), then sequentially stained with 2% uranyl acetate in 50% ethanol for 15 min, and Reynolds' lead citrate for 5 min. Images of autophagic vesicles were acquired using a Tecnai 10 TEM (Philips, Amsterdam,

Table 2 | Spearman correlation coefficients between TFI (2D) and TFI (3D), MFI (2D) and MFI (3D) of PIP-FUCCI cell lines

WT PIP-FUCCI				ATG7 KO PIP-FUCCI			
TFI (3D) of DiD-LIP	TFI (3D) of DiD-LIP	MFI (3D) of DiD-LIP	MFI (3D) of DiD-LIP	TFI (3D) of DiD-LIP	TFI (3D) of DiD-LIP	MFI (3D) of DiD-LIP	MFI (3D) of DiD-LIP
TFI (2D) of DiD-LIP	0.791 ($p < 0.0001$)	/	/	0.715 ($p < 0.0001$)	/	/	/
MFI (2D) of DiD-LIP	/	0.793 ($p < 0.0001$)	/	/	/	0.689 ($p < 0.0001$)	/
TFI (2D) of DiD-LIP	0.872 ($p < 0.0001$)	/	/	0.811 ($p < 0.0001$)	/	/	/
MFI (2D) of DiD-LIP	/	/	0.932 ($p < 0.0001$)	/	/	/	0.905 ($p < 0.0001$)

TFI Total fluorescence intensity, MFI Mean fluorescence intensity, DiD-LIP DiD-labeled liposomes (at a dose equivalent to 5 µg/mL DOX), DiD-LNP DiD-labeled lipid nanoparticles (at a dose equivalent to 6 µg/mL mRNA), 2D Two-dimensional level, 3D Three-dimensional level. The level of significance was set at $p < 0.05$. Source data are provided as a Source Data file.

Table 3 | Spearman correlation coefficients between TFI (2D) and MFI (2D), TFI (3D) and MFI (3D) of PIP-FUCCI cell lines

WT PIP-FUCCI				ATG7 KO PIP-FUCCI			
MFI (2D) of DiD-LIP	MFI (2D) of DiD-LIP	TFI (3D) of DiD-LIP	TFI (3D) of DiD-LIP	MFI (2D) of DiD-LIP	MFI (2D) of DiD-LIP	TFI (3D) of DiD-LIP	TFI (3D) of DiD-LIP
TFI (2D) of DiD-LIP	0.711 ($p < 0.0001$)	/	/	0.699 ($p < 0.0001$)	/	/	/
MFI (3D) of DiD-LIP	/	0.495 ($p < 0.0001$)	/	/	/	0.546 ($p < 0.0001$)	/
TFI (2D) of DiD-LIP	0.918 ($p < 0.0001$)	/	/	0.856 ($p < 0.0001$)	/	/	/
MFI (3D) of DiD-LIP	/	/	0.871 ($p < 0.0001$)	/	/	/	0.791 ($p < 0.0001$)

TFI Total fluorescence intensity, MFI Mean fluorescence intensity, DiD-LIP DiD-labeled liposomes (at a dose equivalent to 5 µg/mL DOX), DiD-LNP DiD-labeled lipid nanoparticles (at a dose equivalent to 6 µg/mL mRNA), 2D Two-dimensional level, 3D Three-dimensional level. The level of significance was set at $p < 0.05$. Source data are provided as a Source Data file.

Netherlands) at 100 kV. 10 cells per group were randomly selected for imaging and statistical analyses.

Western blotting to assess possible effects of nanoparticles on autophagy-related proteins

WT and ATG7 KO PIP-FUCCI cells were seeded at 7×10^5 cells per 6-cm dish and cultured overnight. After treatment with DiD-LIP and DiD-LNP for 2 h, cells were harvested by trypsinization, washed three times with PBS, and lysed in RIPA buffer (containing proteases and phosphatase inhibitors) on ice for 10 min. Protein concentrations were determined using a BCA protein assay kit. Proteins (40 µg/lane) were separated by 15% SDS-PAGE, transferred to a PVDF membrane and blocked with 5% (w/v) bovine serum albumin for 1 h. The membrane was sectioned and incubated overnight at 4 °C with primary antibodies: anti-ATG7 (1:1000), anti-SQSTM1/p62 (1:1000), anti-MAP1LC3A/B (1:1000) and anti-β-actin (1:5000). After washing with TBS containing 0.1% (v/v) Tween 20, membranes were incubated with secondary antibodies (1:5000) for 2 h. Signals were detected using an Odyssey imaging system (LI-COR Biosciences, Lincoln, USA). Related blots have been uploaded as Source Data.

Integration of PIP-FUCCI expression with mitotic shake-off for distinguishment and collection of cells at four cell cycle phases and determination of cell cycle-associated nanoparticle accumulation

WT and ATG7 KO PIP-FUCCI cells were seeded at 8×10^4 cells per confocal dish and cultured overnight. Cells were incubated with DiD-labeled model nanoparticles (blue intracellular fluorescence in CLSM) at designated doses for 2 h. For the final 30 min, 25 µL FITC-EpCAM monoclonal antibody (an epithelial cell adhesion molecule⁷⁴, green fluorescence in CLSM) was added to outline cell membranes and exclude apoptotic cells or cell debris.

To achieve complete separation and adequate collection of cells at four different cell cycle phases, mitotic shake-off was performed to collect floating M-phase cells³⁷ with sterile centrifuge tubes, then the settled and concentrated mitotic cells were transferred into a new confocal dish. Both the adherent G1-phase (mVenus single-positive, green nuclear fluorescence in CLSM), S-phase (mCherry single-positive, red nuclear fluorescence in CLSM), and G2-phase (mVenus and mCherry double-positive, yellow nuclear fluorescence in CLSM) cells remained in the original confocal dish, and the floating M-phase cells (mVenus and mCherry double-positive, yellow nuclear fluorescence in CLSM) transferred into the new dish were gently rinsed three times with PBS to remove unbound fluorophores, before examination with high-resolution CLSM (see the below section). Notably, initially floating M-phase cells were evaluated for intracellular nanoparticle accumulation after they “sitting down” but not “re-adhering” onto the bottom of the culture dish (within 3 min post-transfer). Despite spectral overlap, distinct localization of membrane FITC-EpCAM and nuclear mVenus prevented signal interference^{36,74}.

High-resolution CLSM and 3D reconstruction technique for multi-dimensional evaluation of cell cycle- and autophagy-associated nanoparticle accumulation

The successful construction of WT and ATG7 KO PIP-FUCCI cell lines and the achievement of complete cell cycle phase separation have provided us with the opportunity to simultaneously determine cell cycle- and autophagy-associated cellular accumulation of DiD-labeled model nanoparticles. Live-cell imaging was performed using a Zeiss LSM 880 confocal microscope (Carl Zeiss, Jena, Germany) with a 63×oil objective (NA 1.40, 2048×2048 resolution) in a climate-controlled chamber (37 °C, 5% CO₂). Filter sets were as follows: mVenus (excitation: 514 nm, emission: 519–590 nm), mCherry (excitation: 561 nm, emission: 570–620 nm), DiD (excitation: 633 nm, emission: 638–756 nm) and FITC (excitation: 488 nm, emission: 500–550 nm)³⁶.

In addition to labeling the cell membrane with FITC, morphological examination of the cell with bright field was helpful in identifying typical and healthy M-phase cells with intact and smooth cell membranes.

Cells were randomly selected and imaged by high-resolution CLSM at both two-dimensional (2D) and three-dimensional (3D) levels, with 3D imaging acquiring 30–80 μm z-stacks at z-step intervals of 0.4–1.0 μm . For 2D analyses, cell cycle phases were determined by nuclear fluorescence, and intracellular DiD fluorescence was measured uniformly across groups with cell boundaries delineated by brightfield and FITC signals. Total fluorescence intensity (TFI) of DiD was quantified using Fiji/Image J (NIH, Bethesda, MD, USA), and background fluorescence from the control group was subtracted to yield TFI (2D). To eliminate variations in TFI (2D) due to differences in cell area, mean fluorescence intensity (MFI) at the 2D level, referred to as MFI (2D), was calculated as the ratio of TFI (2D) to cell area⁷⁵. For 3D analyses, 3D reconstructions from confocal z-stacks were generated in Imaris 9.6.1 (Bitplane) with consistent parameters to quantify TFI. Similarly, TFI (3D) was background-corrected and divided by cell volume to yield MFI (3D)⁷⁶.

Detection of cellular accumulation of DiD-LIP in suspended G1-phase, S-phase, G2-phase and M-phase cells

WT and *ATG7* KO PIP-FUCCI cells were seeded at 8×10^4 cells per confocal dish and cultured overnight. Cells were incubated with DiD-LIP at the designated dose for 2 h, with 25 μL FITC-EpCAM antibody added for the final 30 min. Mitotic shake-off was used to collect floating M-phase cells (mVenus and mCherry double-positive, yellow nuclear fluorescence in CLSM)³⁷ with sterile centrifuge tubes, then settled and concentrated mitotic cells were treated with trypsin for 3 min. Adherent G1-phase (mVenus single-positive, green nuclear fluorescence in CLSM), S-phase (mCherry single-positive, red nuclear fluorescence in CLSM) and G2-phase (mVenus and mCherry double-positive, yellow nuclear fluorescence in CLSM) cells remaining in the original dish were dissociated into suspensions with trypsinization in the same manner. Subsequently, suspended G1/S/G2-phase cells and M-phase cells were respectively, collected and transferred to new confocal dishes. Cells were randomly selected and intracellular nanoparticle accumulation was examined using high-resolution CLSM, followed by processing and analyzing images obtained at both 2D and 3D levels (see the above section).

Correlation analyses and inter-group comparisons

Two-tailed Pearson or Spearman correlation analyses were used to assess correlations between TFI (2D) and cell area, TFI (3D) and cell volume, and between multi-dimensional TFI and MFI parameters. Significance was set at $p < 0.05$. The strengths of correlations were assessed using the correlation coefficients (r) (r ranges: 0.00–< 0.30, negligible correlations; 0.30–< 0.50, low correlations; 0.50–< 0.70, moderate correlations; 0.70–< 0.90, high correlations and 0.90–< 1.00, very high correlations)⁷⁷. In addition, inter-group correlation differences were assessed using two-tailed Fisher's z-tests, with $p < 0.05$ considered statistically significant⁷⁸.

Data presentation and statistical analyses

Data were presented as mean \pm SD (normally distributed) or median (IQR) (non-normally distributed), with normality assessed by Shapiro-Wilk tests⁷⁹. Normally distributed data, including Z-average/PDI, cell cycle distribution, and \log_{10} -transformed cell area/cell volume/TFI/MFI, were analyzed by parametric tests (one-way ANOVA followed by Bonferroni multiple comparisons test for multi-group comparisons and two-tailed independent sample t -tests for two-group comparisons), given their higher statistical power⁸⁰. Nonparametric two-tailed Mann-Whitney U tests with Monte Carlo approximation were used to compare autophagic vesicle numbers (non-normally distributed)

between WT and *ATG7* KO PIP-FUCCI cells. All statistical analyses were conducted using SPSS 21.0 (IBM, Chicago, IL, USA). $p < 0.05$ is considered statistically significant.

Reporting summary

Further information on research design is available in the Nature Portfolio Reporting Summary linked to this article.

Data availability

All data supporting the findings of this study are available within the main text and Supplementary Information files. Due to the substantial volume (>1 TB), raw datasets are available from the corresponding author (M.S.) upon request. Source data is available for Figs. 1 and 3–6, Tables 1–3, Supplementary Figs. 1–3, 5, 9, 10, 12, 13, and 15–19, and Supplementary Tables 1–18 in the associated source data file. Source data are provided in this paper.

References

- Caster, J. M., Patel, A. N., Zhang, T. & Wang, A. Investigational nanomedicines in 2016: a review of nanotherapeutics currently undergoing clinical trials. *Wiley Interdiscip. Rev. Nanomed. Nanobiotecnol.* **9**, e1416 (2017).
- Mitchell, M. J. et al. Engineering precision nanoparticles for drug delivery. *Nat. Rev. Drug Discov.* **20**, 101–124 (2021).
- Barenholz, Y. Doxil®-the first FDA-approved nano-drug: lessons learned. *J. Control. Release* **160**, 117–134 (2012).
- Wang, H. Y. et al. Polyethylene glycol (PEG)-associated immune responses triggered by clinically relevant lipid nanoparticles in rats. *NPJ Vaccines* **8**, 169 (2023).
- Zhivotovsky, B. & Orrenius, S. Cell cycle and cell death in disease: past, present and future. *J. Intern. Med.* **268**, 395–409 (2010).
- Abouzeid, A. H. & Torchilin, V. P. The role of cell cycle in the efficiency and activity of cancer nanomedicines. *Expert Opin. Drug De.* **10**, 775–786 (2013).
- Sui, M. H., Dziadyk, J. M., Zhu, X. M. & Fan, W. M. Cell cycle-dependent antagonistic interactions between paclitaxel and γ -radiation in combination therapy. *Clin. Cancer Res.* **10**, 4848–4857 (2004).
- Sui, M. H. & Xiong, X. X. Combination of gemcitabine antagonizes antitumor activity of paclitaxel through prevention of mitotic arrest and apoptosis. *Cancer Biol. Ther.* **5**, 1015–1021 (2006).
- Sui, M. H. et al. G2 checkpoint abrogator abates the antagonistic interaction between antimicrotubule drugs and radiation therapy. *Radiother. Oncol.* **104**, 243–248 (2012).
- Zhang, R., Yang, J. Y., Sima, M., Zhou, Y. & Kopeček, J. Sequential combination therapy of ovarian cancer with degradable N-(2-hydroxypropyl) methacrylamide copolymer paclitaxel and gemcitabine conjugates. *Proc. Natl. Acad. Sci. USA* **111**, 12181–12186 (2014).
- Zheng, S. et al. Effects of cell cycle on the uptake of water soluble quantum dots by cells. *J. Appl. Phys.* **110**, 124701 (2011).
- Wu, J. et al. Statistical single-cell analysis of cell cycle-dependent quantum dot cytotoxicity and cellular uptake using microfluidic system. *RSC Adv.* **4**, 24929–24934 (2014).
- Rees, P., Wills, J. W., Brown, M. R., Barnes, C. M. & Summers, H. D. The origin of heterogeneous nanoparticle uptake by cells. *Nat. Commun.* **10**, 2341 (2019).
- Wang, Z. et al. Efficient delivery of biological cargos into primary cells by electrodeposited nanoneedles via cell-cycle-dependent endocytosis. *Nano Lett.* **23**, 5877–5885 (2023).
- Patel, P. et al. Cell cycle dependent cellular uptake of zinc oxide nanoparticles in human epidermal cells. *Mutagenesis* **31**, 481–490 (2016).
- Kim, J. A., Åberg, C., Salvati, A. & Dawson, K. A. Role of cell cycle on the cellular uptake and dilution of nanoparticles in a cell population. *Nat. Nanotechnol.* **7**, 62–68 (2012).

17. Panet, E. et al. The interface of nanoparticles with proliferating mammalian cells. *Nat. Nanotechnol.* **12**, 598–600 (2017).
18. Åberg, C., Kim, J. A., Salvati, A. & Dawson, K. A. Reply to 'The interface of nanoparticles with proliferating mammalian cells'. *Nat. Nanotechnol.* **12**, 600–603 (2017).
19. Go, E. J., Kim, E. J. & Hur, W. In vitro cellular uptake of fibroin microspheres and its dependency on the cell cycle stage. *J. Microencapsul.* **30**, 124–131 (2013).
20. Huang, C. et al. Altered cell cycle arrest by multifunctional drug-loaded enzymatically-triggered nanoparticles. *ACS Appl. Mater. Interfaces* **8**, 1360–1370 (2016).
21. Tang, J. H. et al. The role of the cell cycle in the cellular uptake of folate-modified poly(L-amino acid) micelles in a cell population. *Nanoscale* **7**, 20397–20404 (2015).
22. Su, L. J. et al. GRP75-driven, cell-cycle-dependent macro-pinocytosis of Tat/pDNA-Ca²⁺ nanoparticles underlies distinct gene therapy effect in ovarian cancer. *J. Nanobiotechnol.* **20**, 340 (2022).
23. Li, X. H., He, S. K. & Ma, B. Y. Autophagy and autophagy-related proteins in cancer. *Mol. Cancer* **19**, 12 (2020).
24. Akin, D. et al. A novel ATG4B antagonist inhibits autophagy and has a negative impact on osteosarcoma tumors. *Autophagy* **10**, 2021–2035 (2014).
25. Yang, S. H. et al. Pancreatic cancers require autophagy for tumor growth. *Genes Dev.* **25**, 717–729 (2011).
26. Collier, J. J. et al. Emerging roles of ATG7 in human health and disease. *Embo. Mol. Med.* **13**, e14824 (2021).
27. Manzanera, D. & Ceña, V. Endocytosis: the nanoparticle and sub-micron nanocompounds gateway into the cell. *Pharmaceutics* **12**, 371 (2020).
28. Birgisdottir, Å. & Johansen, T. Autophagy and endocytosis-interconnections and interdependencies. *J. Cell Sci.* **133**, jcs228114 (2020).
29. Zheng, W., Wei, M., Li, S. & Le, W. Nanomaterial-modulated autophagy: underlying mechanisms and functional consequences. *Nanomedicine* **11**, 1417–1430 (2016).
30. Fageria, L. et al. Functional autophagic flux regulates AgNP uptake and the internalized nanoparticles determine tumor cell fate by temporally regulating flux. *Int. J. Nanomed.* **14**, 9063–9076 (2019).
31. Sipo, A. et al. Alveolar epithelial cell processing of nanoparticles activates autophagy and lysosomal exocytosis. *Am. J. Physiol. Lung Cell. Mol. Physiol.* **315**, L286–L300 (2018).
32. Sipo, A., Kim, K. J., Sioutas, C. & Crandall, E. D. Evidence for nanoparticle-induced lysosomal dysfunction in lung adenocarcinoma (A549) cells. *Int. J. Mol. Sci.* **20**, 5253 (2019).
33. Guo, Q. et al. Hollow MIL-125 nanoparticles loading doxorubicin prodrug and 3-Methyladenine for reversal of tumor multidrug resistance. *J. Funct. Biomater.* **14**, 546 (2023).
34. Yang, Y. P. et al. Application and interpretation of current autophagy inhibitors and activators. *Acta Pharmacol. Sin.* **34**, 625–635 (2013).
35. Park, E. J. et al. Chloroquine enhances TRAIL-mediated apoptosis through up-regulation of DR5 by stabilization of mRNA and protein in cancer cells. *Sci. Rep.* **6**, 22921 (2016).
36. Grant, G. D. et al. Accurate delineation of cell cycle phase transitions in living cells with PIP-FUCCI. *Cell Cycle* **17**, 2496–2516 (2018).
37. Jackman, J. & O'Connor, P. M. Methods for synchronizing cells at specific stages of the cell cycle. *Curr. Protoc. Cell Biol.* **8**, 8.3.1–8.3.20 (1998).
38. Doxil prescribing information. https://www.accessdata.fda.gov/drugsatfda_docs/label/2022/050718Orig1s060lbl.pdf (2022).
39. Comirnaty prescribing information. <https://labeling.pfizer.com/ShowLabeling.aspx?id=16351&format=pdf> (2021).
40. Liu, R. F., Tang, J., Xu, Y. X. & Dai, Z. F. Bioluminescence imaging of inflammation in vivo based on bioluminescence and fluorescence resonance energy transfer using nanobubble ultrasound contrast agent. *ACS Nano* **13**, 5124–5132 (2019).
41. Yang, L. et al. Live macrophage-delivered doxorubicin-loaded liposomes effectively treat triple-negative breast cancer. *ACS Nano* **16**, 9799–9809 (2022).
42. Khare, P. et al. Lipid nanoparticle-mediated drug delivery to the brain. *Adv. Drug Deliv. Rev.* **197**, 114861 (2023).
43. Cadart, C. et al. Exploring the function of cell shape and size during mitosis. *Dev. Cell* **29**, 159–169 (2014).
44. Taubenberger, A. V., Baum, B. & Matthews, H. K. The mechanics of mitotic cell rounding. *Front. Cell Dev. Biol.* **8**, 687 (2020).
45. Wise, G. E. & Prescott, D. M. Initiation and continuation of DNA replication are not associated with the nuclear envelope in mammalian cells. *Proc. Natl. Acad. Sci. USA* **70**, 714–717 (1973).
46. Schorl, C. & Sedivy, J. M. Analysis of cell cycle phases and progression in cultured mammalian cells. *Methods* **41**, 143–150 (2007).
47. Li, T. et al. Phosphorylation and chromatin tethering prevent cGAS activation during mitosis. *Science* **371**, eabc5386 (2021).
48. Dulla, K. et al. Quantitative site-specific phosphorylation dynamics of human protein kinases during mitotic progression. *Mol. Cell Proteom.* **9**, 1167–1181 (2010).
49. Ullah, M. et al. Mitosis in cancer cell increases immune resistance via high expression of HLA-G and PD-L1. *Cancers* **12**, 2661 (2020).
50. Costa, A. C. et al. *Listeria monocytogenes* interferes with host cell mitosis through its virulence factors InlC and ActA. *Toxins* **12**, 411 (2020).
51. Jonkman, J. et al. Tutorial: guidance for quantitative confocal microscopy. *Nat. Protoc.* **15**, 1585–1611 (2020).
52. Kessel, D. H., Price, M. & Reiners, J. J. Jr ATG7 deficiency suppresses apoptosis and cell death induced by lysosomal photodamage. *Autophagy* **8**, 1333–1341 (2012).
53. Li, W. et al. Phospholipid peroxidation inhibits autophagy via stimulating the delipidation of oxidized LC3-PE. *Redox Biol.* **55**, 102421 (2022).
54. Needham, D. Possible role of cell cycle-dependent morphology, geometry, and mechanical properties in tumor cell metastasis. *Cell Biophys.* **18**, 99–121 (1991).
55. Wang, Z. X. Regulation of cell cycle progression by growth factor-induced cell signaling. *Cells* **10**, 3327 (2021).
56. Raucher, D. & Sheetz, M. P. Membrane expansion increases endocytosis rate during mitosis. *J. Cell Biol.* **144**, 497–506 (1999).
57. Alber, A. B. & Suter, D. M. Dynamics of protein synthesis and degradation through the cell cycle. *Cell Cycle* **18**, 784–794 (2019).
58. Li, Y. et al. APC/C^{CDH1} synchronizes ribose-5-phosphate levels and DNA synthesis to cell cycle progression. *Nat. Commun.* **10**, 2502 (2019).
59. Antonescu, C. N., McGraw, T. E. & Klip, A. Reciprocal regulation of endocytosis and metabolism. *Cold Spring Harb. Perspect. Biol.* **6**, a016964 (2014).
60. Zheng, Y., Su, C., Zhao, L. & Shi, Y. J. Chitosan nanoparticle-mediated co-delivery of shAtg-5 and gefitinib synergistically promoted the efficacy of chemotherapeutics through the modulation of autophagy. *J. Nanobiotechnol.* **15**, 28 (2017).
61. Hu, C. L. et al. Co-delivery of the autophagy inhibitor si-Beclin1 and the doxorubicin nano-delivery system for advanced prostate cancer treatment. *J. Biomater. Appl.* **36**, 1317–1331 (2022).
62. Chen, J. L. et al. Autophagy inhibitors for cancer therapy: Small molecules and nanomedicines. *Pharmacol. Ther.* **249**, 108485 (2023).
63. Cespedes Feliciano, E. M. et al. Body composition, adherence to anthracycline and taxane-based chemotherapy, and survival after nonmetastatic breast cancer. *JAMA Oncol.* **6**, 264–270 (2020).
64. Bavli, Y. et al. Doxebo (doxorubicin-free Doxil-like liposomes) is safe to use as a pre-treatment to prevent infusion reactions to PEGylated nanodrugs. *J. Control. Release* **306**, 138–148 (2019).
65. Zhang, N. N. et al. A thermostable mRNA vaccine against COVID-19. *Cell* **182**, 1271–1283 (2020).

66. Stewart, J. C. M. Colorimetric determination of phospholipids with ammonium ferrothiocyanate. *Anal. Biochem.* **104**, 10–14 (1980).
67. Bandyopadhyay, A., McCarthy, K. A., Kelly, M. A. & Gao, J. Targeting bacteria via iminoboronate chemistry of amine-presenting lipids. *Nat. Commun.* **6**, 6561 (2015).
68. Li, Y. J. et al. Thermal-responsive carbon monoxide (CO) delivery expedites metabolic exhaustion of cancer cells toward reversal of chemotherapy resistance. *ACS Cent. Sci.* **5**, 1044–1058 (2019).
69. Shi, C. Y. et al. A drug-specific nanocarrier design for efficient anticancer therapy. *Nat. Commun.* **6**, 7449 (2015).
70. Parhiz, H. et al. PECAM-1 directed re-targeting of exogenous mRNA providing two orders of magnitude enhancement of vascular delivery and expression in lungs independent of apolipoprotein E-mediated uptake. *J. Control. Release* **291**, 106–115 (2018).
71. Paunovska, K. et al. Increased PIP3 activity blocks nanoparticle mRNA delivery. *Sci. Adv.* **6**, 5672 (2020).
72. Maugeri, M. et al. Linkage between endosomal escape of LNP-mRNA and loading into EVs for transport to other cells. *Nat. Commun.* **10**, 4333 (2019).
73. McGarry, T. J. & Kirschner, M. W. Geminin, an inhibitor of DNA replication, is degraded during mitosis. *Cell* **93**, 1043–1053 (1998).
74. Jing, Y. Y. et al. Quantitatively mapping the assembly pattern of EpCAM on cell membranes with peptide probes. *Anal. Chem.* **92**, 1865–1873 (2020).
75. Shen, X. et al. MiR-322/-503 rescues myoblast defects in myotonic dystrophy type 1 cell model by targeting CUG repeats. *Cell Death Dis.* **11**, 891 (2020).
76. Trivedi, P. et al. The inner centromere is a biomolecular condensate scaffolded by the chromosomal passenger complex. *Nat. Cell Biol.* **21**, 1127–1137 (2019).
77. Mukaka, M. M. Statistics corner: a guide to appropriate use of correlation coefficient in medical research. *Malawi Med. J.* **24**, 69–71 (2012).
78. Abeler-Dörner, L. et al. High-throughput phenotyping reveals expansive genetic and structural underpinnings of immune variation. *Nat. Immunol.* **21**, 86–100 (2020).
79. Nguyen, S. et al. Elite control of HIV is associated with distinct functional and transcriptional signatures in lymphoid tissue CD8⁺ T cells. *Sci. Transl. Med.* **11**, eaax4077 (2019).
80. Nahm, F. S. Nonparametric statistical tests for the continuous data: the basic concept and the practical use. *Korean J. Anesthesiol.* **69**, 8–14 (2016).

Acknowledgements

This work was supported by grants from Zhejiang Provincial Natural Science Foundation of China (LZ23E030003 to M.S.), the National Natural Science Foundation of China (22075243 and 21722405 to M.S.), National Key R&D Program of China (2022YFC2704200 and 2022YFC2704203 to X.C. and M.S.), and Startup Foundation for Hundred-Talent Program of Zhejiang University (to M.S.). We would like to acknowledge Dr. Yingjie Wang, Dr. Wei Liu, Dr. Yongzhong Du and Dr. Qiming Sun at Zhejiang University for insightful discussions. In addition, we would like to acknowledge Shenghai Chang, Lingyun Wu and Beibei Wang in the Center of Cryo-Electron Microscopy (CCEM), Zhejiang University for their technical assistance on Cryo-EM and TEM. We would

like to acknowledge Shuangshuang Liu, Guifeng Xiao and Yueting Xing from the Core Facilities, Zhejiang University School of Medicine, for their technical assistance on confocal live imaging, 3D reconstruction and flow cytometry. We would also like to acknowledge Yina Wang for her assistance on language polishing.

Author contributions

M.S., the principal investigator of the major supporting grants, and Y.W. conceived the study and defined the goals of the present study. M.S., Y.W., G.L., and H.W. designed the experiments. Y.W., G.L., and H.W. performed the research. X.X. provided technical/platform supports. M.S., Y.W., G.L., H.W., Y.Z., W.Z., J.L., B.C., Y.G., and Y.J. discussed this project and analyzed the data. M.S., Y.W., G.L., and H.W. drafted the manuscript. M.S., Y.W., G.L., H.W., Y.Z., W.Z., J.L., B.C., Y.G., and Y.J. revised and edited the manuscript. These authors contributed equally: Y.W., G.L., and H.W.

Competing interests

The authors declare no competing interests

Additional information

Supplementary information The online version contains supplementary material available at <https://doi.org/10.1038/s41467-025-60962-4>.

Correspondence and requests for materials should be addressed to Meihua Sui.

Peer review information *Nature Communications* thanks the anonymous reviewers for their contribution to the peer review of this work. A peer review file is available.

Reprints and permissions information is available at <http://www.nature.com/reprints>

Publisher's note Springer Nature remains neutral with regard to jurisdictional claims in published maps and institutional affiliations.

Open Access This article is licensed under a Creative Commons Attribution-NonCommercial-NoDerivatives 4.0 International License, which permits any non-commercial use, sharing, distribution and reproduction in any medium or format, as long as you give appropriate credit to the original author(s) and the source, provide a link to the Creative Commons licence, and indicate if you modified the licensed material. You do not have permission under this licence to share adapted material derived from this article or parts of it. The images or other third party material in this article are included in the article's Creative Commons licence, unless indicated otherwise in a credit line to the material. If material is not included in the article's Creative Commons licence and your intended use is not permitted by statutory regulation or exceeds the permitted use, you will need to obtain permission directly from the copyright holder. To view a copy of this licence, visit <http://creativecommons.org/licenses/by-nc-nd/4.0/>.

© The Author(s) 2025